Title

The GPCR—Gαs—PKA signaling axis promotes T cell dysfunction and cancer immunotherapy failure

Journal

Nature Immunology, 24(8)

ISSN

1529-2908

Authors

Wu, Victoria H

Yung, Bryan S

Faraji, Farhoud

et al.

Publication Date

2023-08-01

DOI

10.1038/s41590-023-01529-7

Peer reviewed

HHS Public Access

Author manuscript

Nat Immunol. Author manuscript; available in PMC 2023 December 21.

Published in final edited form as:

Nat Immunol. 2023 August ; 24(8): 1318–1330. doi:10.1038/s41590-023-01529-7.

The GPCR–$G\alpha_s$–PKA signaling axis promotes T cell dysfunction and cancer immunotherapy failure

Victoria H. Wu[1,13,15], **Bryan S. Yung**[1,15], **Farhoud Faraji**[2,3], **Robert Saddawi-Konefka**[2,3], **Zhiyong Wang**[3], **Alexander T. Wenzel**[3,4], **Miranda J. Song**[3,4], **Meghana S. Pagadala**[4], **Lauren M. Clubb**[1], **Joshua Chiou**[5,14], **Sanju Sinha**[6], **Marin Matic**[7], **Francesco Raimondi**[7], **Thomas S. Hoang**[1], **Rebecca Berdeaux**[8], **Dario A. A. Vignali**[9,10,11], **Ramiro Iglesias-Bartolome**[12], **Hannah Carter**[3,4], **Eytan Ruppin**[6], **Jill P. Mesirov**[3,4], **J. Silvio Gutkind**[1,✉]

[1]Department of Pharmacology, UCSD Moores Cancer Center, University of California, San Diego, La Jolla, CA, USA.

[2]Department of Otolaryngology—Head and Neck Surgery, University of California San Diego Health, La Jolla, CA, USA.

[3]UCSD Moores Cancer Center, University of California, San Diego, La Jolla, CA, USA.

[4]Department of Medicine, University of California, San Diego, La Jolla, CA, USA.

[5]Biomedical Sciences Graduate Studies Program, University of California, San Diego, La Jolla, CA, USA.

[6]Cancer Data Science Laboratory, Center for Cancer Research, National Cancer Institute, National Institutes of Health, Bethesda, MD, USA.

[7]Laboratorio di Biologia Bio@SNS, Scuola Normale Superiore, Pisa, Italy.

✉**Correspondence and requests for materials** should be addressed to J. Silvio Gutkind. sgutkind@health.ucsd.edu.

Author contributions

V.H.W. and B.S.Y. designed and conceived the studies, conducted most experiments described in this study and interpreted the data. F.F., Z.W. and R.S.-K. performed experiments described in the study. A.T.W., M.J.S., M.S.P., L.M.C., J.C., S.S., M.M., F.R., H.C., E.R. and J.P.M. all contributed to the bioinformatics analysis of this project. V.H.W., B.S.Y., F.F., R.S.-K., T.S.H., D.A.A.V., R.I.-B., R.B. and J.S.G. contributed to the study design and writing of the manuscript. J.S.G. provided oversight and direction of the entire project and study design, provided financial support for the study, interpreted the data and wrote the manuscript.

Online content

Any methods, additional references, Nature Portfolio reporting summaries, source data, extended data, supplementary information, acknowledgements, peer review information; details of author contributions and competing interests; and statements of data and code availability are available at https://doi.org/10.1038/s41590-023-01529-7.

Reporting summary

Further information on research design is available in the Nature Port-folio Reporting Summary linked to this article.

Competing interests

J.S.G. reports consulting fees from Domain Pharmaceuticals, Pangea Therapeutics and io9 and is founder of Kadima Pharmaceuticals, unrelated to the current study. R.B. is an employee and shareholder of CellChorus, Inc. J.C. is an employee and shareholder of Pfizer, Inc. V.H.W. is an employee and shareholder of Septerna, Inc. The other authors declare no competing interests.

Additional information

Extended data is available for this paper at https://doi.org/10.1038/s41590-023-01529-7.

Supplementary information The online version contains supplementary material available at https://doi.org/10.1038/s41590-023-01529-7.

Peer review information *Nature Immunology* thanks William Murphy, Carla Rothlin, and the other, anonymous, reviewer(s) for their contribution to the peer review of this work. Primary Handling Editor: N. Bernard, in collaboration with the *Nature Immunology* team.

[8]Department of Integrative Biology and Pharmacology, McGovern Medical School at UT Health Houston and CellChorus INC, Houston, TX, USA.

[9]Department of Immunology, University of Pittsburgh School of Medicine, Pittsburgh, PA, USA.

[10]Tumor Microenvironment Center, UPMC Hillman Cancer Center, Pittsburgh, PA, USA.

[11]Cancer Immunology and Immunotherapy Program, UPMC Hillman Cancer Center, Pittsburgh, PA, USA.

[12]Laboratory of Cellular and Molecular Biology, Center for Cancer Research, National Cancer Institute, National Institute of Health, Bethesda, MD, USA.

[13]Present address: Septerna, Inc., South San Francisco, CA, USA.

[14]Present address: Internal Medicine Research Unit, Pfizer Worldwide Research, Cambridge, MA, USA.

[15]These authors contributed equally: Victoria H. Wu, Bryan S. Yung.

Abstract

Immune checkpoint blockade (ICB) targeting PD-1 and CTLA-4 has revolutionized cancer treatment. However, many cancers do not respond to ICB, prompting the search for additional strategies to achieve durable responses. G-protein-coupled receptors (GPCRs) are the most intensively studied drug targets but are underexplored in immuno-oncology. Here, we cross-integrated large singe-cell RNA-sequencing datasets from $CD8^+$ T cells covering 19 distinct cancer types and identified an enrichment of $G\alpha_s$-coupled GPCRs on exhausted $CD8^+$ T cells. These include EP_2, EP_4, $A_{2A}R$, β_1AR and β_2AR, all of which promote T cell dysfunction. We also developed transgenic mice expressing a chemogenetic CD8-restricted $G\alpha_s$–DREADD to activate CD8-restricted $G\alpha_s$ signaling and show that a $G\alpha_s$–PKA signaling axis promotes $CD8^+$ T cell dysfunction and immunotherapy failure. These data indicate that $G\alpha_s$–GPCRs are druggable immune checkpoints that might be targeted to enhance the response to ICB immunotherapies.

Breakthrough discoveries over the past few decades have begun to unravel the complexity of the antitumor immune response, leading to the implementation of cancer immunotherapy in humans[1,2]. Specifically, immune checkpoint blockade (ICB) by antibodies targeting programmed cell death protein 1 (PD-1; for example, nivolumab, pembrolizumab and cemiplimab), its ligand programmed death ligand 1 (PD-L1; for example, atezolizumab, avelumab and durvalumab) and CTLA-4 (ipilimumab and tremelimumab) has been approved for multiple cancer types[3,4]. As monotherapies, these checkpoint inhibitors have shown remarkable efficacy in a subset of individuals, but responsiveness is restricted to certain tumor types, and many individuals who initially respond do not have subsequent durable tumor control[5]. This raises the possibility that additional immune checkpoints may exist, which prevent ICB from achieving its full potential and leads to primary or acquired resistance. In this regard, tumors may deploy multiple immune evasion strategies to bypass antitumor immune responses that may need to be blocked concomitantly with ICB to achieve durable tumor remission.

G-protein-coupled receptors (GPCRs) represent the largest family of cell surface receptors involved in signal transduction and are the target of >30% of all Food and Drug Administration-approved drugs[6]. GPCRs have remained the most pharmacologically favorable drug targets primarily due to their druggability and relevance to a broad spectrum of physiological processes and highly prevalent disease conditions[6]. However, the role of GPCRs in immuno-oncology is under-studied; while aberrant GPCR signaling has been implicated in cancer, their roles and expression patterns on tumor-infiltrating immune cells and potential as a target for immunotherapies are less understood[7,8]. There are 800 known human GPCRs, and their signaling cascades are primarily determined by the activation of one or multiple heterotrimeric Gα proteins (for example, $G\alpha_s$, $G\alpha_{i/o}$, $G\alpha_{q/11}$ and $G\alpha_{12/13}$)[9]. The nature of the immune cell infiltrating the tumor microenvironment (TME) is largely dictated by chemokines and their associated GPCRs that guide and recruit different pro- or antitumoral immune cells to the tumor, thereby orchestrating the balance between cytotoxicity and immunosuppression[8]. Most chemokine receptors are coupled to $G\alpha_i$, inhibiting cyclic AMP (cAMP) production. These include CXCR3, a $G\alpha_i$-coupled GPCR on T cells that binds three chemokines (CXCL9, CXCL10 and CXCL11) to promote the migration of T cells into the tumor[10]. These chemokines are induced by interferon-α (IFNα), IFNβ and IFNγ and are part of the IFN gene signature that has predictive value for a favorable response to pembrolizumab[11].

In contrast to these antitumor chemokine receptors, other GPCRs expressed on T cells may override chemokine-coordinated intratumoral cytotoxic T lymphocyte migration and instead display immunosuppressive functions. In this regard, metabolites and inflammatory mediators that accumulate in the TME, such as adenosine and prostaglandins, act on $G\alpha_s$-coupled receptors and display immunosuppressive activity[12,13], albeit their direct impact on $CD8^+$ T cells has not been fully elucidated as their respective receptors are expressed in multiple innate and adaptive immune cell types.

Here, we develop a computational pipeline to integrate large datasets of intratumoral T cell single-cell RNA sequencing (scRNA-seq) and combine it with a synthetic biology approach to show that activation of $G\alpha_s$-coupled GPCRs and the $G\alpha_s$ signaling axis is sufficient to drive a hyporesponsive T cell state. In turn, our findings reveal that concomitant inhibition of $G\alpha_s$-coupled GPCRs with ICB might be necessary to reactivate the antitumor immune response, thereby providing a multimodal immunotherapy approach for cancer treatment.

Results

$G\alpha_s$-coupled GPCR expression and T cell dysfunction

Building on our previous analysis shedding light on the onco-GPCRome and aberrant GPCR signaling and activity on tumor cells[8], we investigated the landscape of GPCR expression on each tumor-infiltrating $CD8^+$ T cell subtype. We collected data and performed an integrated analysis of scRNA-seq datasets from 19 cancer types (Fig. 1a and Supplementary Table 1a). The cancer types covered in this analysis encompass those in which individuals show higher (for example, ~25–50% in non-small cell lung cancer and cutaneous melanoma) and lower (for example, <20% in ovarian cancer and pancreatic cancer) response rates to immunotherapy[14] and thus provide a comprehensive overview of the expression landscape

of tumor-infiltrating CD8$^+$ T cells. Using the Seurat SCTransform scRNA-seq integration method, we jointly analyzed 217,953 total CD8$^+$ T cells, which were stratified into naive, proliferating, cytotoxic, effector memory and exhausted subtypes based on landmark genes and nearest neighbor analysis, ProjecTIL[15] (Fig. 1b,c, Extended Data Fig. 1a,b and Supplementary Table 1b). This resulted in delineation of functional (cytotoxic and effector memory) and dysfunctional (exhausted) CD8$^+$ subtypes, nonspecific naive T cells that stochastically migrate through the tumor and proliferating T cells that express features of both effector memory and exhausted T cells[16,17]. When we analyzed the relative expression of 386 non-olfactory GPCR genes, many GPCRs showed a distinct expression pattern in each CD8$^+$ T cell subtype (Fig. 1d and Supplementary Tables 1c,d). Terminally exhausted CD8$^+$ T cells in both cancer and chronic viral infection most commonly have been shown to express high levels of PD-1, TIM-3, CXCR6, LAG3, CTLA-4 and CXCL13 proteins, all of which are reflected at the transcriptomic level in our combined analysis, as previously documented and validated in the individual datasets (Supplementary Table 1a–c). Within exhausted CD8$^+$ T cells, we found that *CXCR6*, *PTGER4*, *GPR65*, *ADGRE5* and *F2R* were among the most highly expressed genes encoding GPCRs, with expression patterns similar to those of signature exhaustion genes (Fig. 1e).

A transcriptional gene module predicting T cell dysfunction programs linked to *LAG3* expression (for example, *TIGIT*, *PDCD1*, *LAG3* and *CXCL13*) was established in individuals with melanoma[18]. To identify GPCRs most relevant to this dysfunction program, we generated dysfunction scores for all CD8$^+$ T cells from our integrated analyses (Fig. 1f and Supplementary Table 1e). As expected, exhausted CD8$^+$ Tcells across 19 cancer types displayed the highest dysfunction scores, significantly higher than proliferating, cytotoxic and effector memory CD8$^+$ T cells (Fig. 1g and Extended Data Fig. 1c). We next investigated the GPCR genes most strongly associated with T cell dysfunction scores. The gene encoding CXCR6, which is expressed on PD-1^{hi} effector and exhausted CD8$^+$ Tcells during chronic viral infection, was the GPCR gene most significantly correlated with Tcell dysfunction[19] (Fig. 1h). In total, 35 GPCR genes were shown to be significantly correlated with the dysfunction score, with *GPR56*, *CCRL2*, *GIPR* and *F2R* among the top candidates to contribute to Tcell exhaustion (Fig. 1h and Supplementary Table 2a). We next aimed to distinguish GPCR expression patterns based on heterotrimeric G-protein coupling information to begin defining functional gene sets. Based on the International Union of Basic and Clinical Pharmacology (IUPHAR) classification, we grouped all GPCRs into G-protein programs based on their primary G-protein coupling to $G\alpha_{12/13}$, $G\alpha_i$, $G\alpha_{q/11}$ or $G\alpha_s$ (Supplementary Table 2b). Intriguingly, when we calculated the mean correlation of each pathway, we found that the $G\alpha_s$ program was the most enriched with Tcelldysfunction, while the $G\alpha_i$ programwasthe leastcorrelated(Fig. 1i). Multiple genes encoding $G\alpha_s$-coupled GPCRs were positively correlated with Tcell dysfunction with significant Spearman correlations, including *GIPR*, *ADORA2A*, *PTGER4*, *GPR65* and *TSHR* (Fig. 1j). These data raise the possibility of a GPCR–$G\alpha_s$ signaling program that correlates with T cell dysfunction in tumor-infiltrating CD8$^+$ T cells.

Endogenous $G\alpha_s$–GPCRs diminish effector T cell function

Next, we investigated the relevance of $G\alpha_s$–GPCRs to exhausted T cell phenotypes. We analyzed bulk transcriptomic data from the mouse lymphocytic choriomeningitis virus (LCMV) chronic infection model, which represents the experimental model system most central to recent landmark discoveries defining T cell exhaustion[20] (Fig. 2a and Supplementary Table 3a). In this model, acute infection with a strain of LCMV (Armstrong) generates robust, proliferative and activated effector $CD8^+$ T cells that are able to resolve infection[21]. By contrast, chronic infection with a different strain of LCMV (clone 13) leads to persistent antigen exposure, generating a distinct exhausted T cell state with sustained expression of inhibitory receptors and hierarchical loss of effector functions[21]. We combined three RNA-seq datasets of fluorescence-activated cell sorting-purified effector $CD8^+$ T cells from acute LCMV infection and exhausted T cells from chronic LCMV infection and used DESeq2 to directly compare differential expression of GPCRs between the two $CD8^+$ T cell subtypes. This revealed that multiple genes encoding $G\alpha_s$–GPCRs are upregulated in exhausted T cells compared to in effector T cells, including *Glp1r*, *Ptger2*, *Ptger4* and *Gpr65*, which are also significantly correlated with T cell dysfunction in human tumor-infiltrating $CD8^+$ T cells (Figs. 1g and 2b and Supplementary Table 3b). This suggests that the $G\alpha_s$–GPCRs that are expressed on both exhausted tumor-infiltrating $CD8^+$ T cells and exhausted $CD8^+$ T cells during chronic viral infection are intrinsically similar.

Recently, we have determined coupling across 148 human GPCRs for 11 specific human G proteins and used a machine learning approach to augment GPCR coupling predictions for class A GPCRs[22]. Here, we curated gene sets stratifying for their predictive G-protein coupling as designated by IUPHAR and our reported assay. We found that the $G\alpha_s$ coupling gene set by IUPHAR had the most significant enrichment with upregulated GPCRs on exhausted T cells in LCMV infection (Fig. 2c). Additional gene sets were also significantly enriched for upregulated GPCRs on exhausted T cells, including GNAQ predicted coupling, $G_{q/11}$ primary IUPHAR coupling and GNA14 predicted coupling (Fig. 2d and Supplementary Table 3c). Together, this suggests that, in addition to T cell dysfunction, the expression of these $G\alpha_s$-coupled GPCRs may also play a role in driving T cell exhaustion.

To gain a better understanding of how the expression of these $G\alpha_s$–GPCRs modulate $CD8^+$ T cells, we first sought to model impairment of T cell function resulting from persistent T cell antigen receptor (TCR) signaling by modulating T cell activation in vitro (Fig. 2e). $CD8^+$ T cells from splenocytes of C57BL/6 mice were activated with anti-CD3 and anti-CD28 for 48 h. Subsequently, cells were subjected to additional restimulation (chronic stimulation) to model reactivation of T cells after TCR engagement at the tumor. As a control, $CD8^+$ T cells were also expanded in culture with interleukin-2 (IL-2; activated) without additional restimulation. Characteristic of terminally exhausted cells, the expression levels of PD-1, CTLA-4, TIM-3 and LAG3 on $CD8^+$ T cells were all significantly elevated in chronically versus acutely stimulated $CD8^+$ T cells, concomitant with a decrease in IFNγ and tumor necrosis factor (TNF), confirming in this assay that chronically activated $CD8^+$ T cells begin acquiring an exhaustion-like phenotype (Extended Data Fig. 2a).

To simulate exposure of $G\alpha_s$ ligands at the TME, we added ligands stimulating $G\alpha_s$–GPCRs to our chronic exhaustion assay (prostaglandin E_2 (PGE_2) for EP_2 and EP_4, dobutamine for β_1 adrenergic receptor (β_1-AR) and β_2AR and CGS-21680 for adenosine 2A receptor ($A_{2A}R$)). After 48 h of the initial activation, $CD8^+$ T cells were replated for an additional 48 h of activation with or without $G\alpha_s$ ligands, and we measured the functional capacity by flow cytometric analysis of IFNγ, TNF and granzyme B. Continuous stimulation and the addition of PGE_2, dobutamine or CGS-21680 all significantly reduced IFNγ, TNF and granzyme B single positivity and highly cytotoxic polyfunctional $CD8^+$ T cells, as measured by cells expressing both IFNγ and TNF (Fig. 2f,g and Extended Data Fig. 2b). A similar reduction was seen in the viability and proliferative capacity of $CD8^+$ T cells, as indicated by the reduction in Ki-67 positivity (Extended Data Fig. 2c). Moreover, stimulation with PGE_2 and dobutamine significantly elevated PD-1 and TIM-3 expression (Fig. 2g and Extended Data Fig. 2d). The simultaneous reduction in T cell function and proliferation and increase of inhibitory receptor expression suggest that $G\alpha_s$ ligands augment the dysfunctional phenotypes in $CD8^+$ T cells polarizing toward exhaustion.

To evaluate the functional suppression by $G\alpha_s$ ligands on cytotoxic T cell killing, we activated purified T cells from OT-1 transgenic mice whose TCRs are specific for the ovalbumin (OVA) peptide SIINFEKL ($OVA_{257–264}$) and cocultured them with MC38 tumor cells expressing OVA (MC38-OVA) at a 1:5 effector:target ratio (Fig. 2h). $G\alpha_s$ ligands significantly diminished the cytotoxicity of OT-1 $CD8^+$ T cells toward MC38-OVA cells as measured by tumor cell viability after 2 d (Fig. 2i). Together, our in vitro experiments identify an inhibitory effect of ligands for $G\alpha_s$–GPCRs on T cell function and cytotoxicity.

To elucidate the underlying mechanisms of $G\alpha_s$-mediated $CD8^+$ T cell dysfunction, we next characterized the pathways downstream of $G\alpha_s$/cAMP that drive immune suppression and focused on PGE_2, as this inflammatory mediator led to the most pronounced inhibition of function from all $G\alpha_s$–GPCR ligands tested. Addition of PGE_2 and forskolin (fsk), a direct adenylyl cyclase-cAMP activator, during chronic stimulation led to a significant increase of the cAMP response element-binding protein (CREB), which becomes phosphorylated (pCREB) following increased intracellular cAMP and protein kinase A (PKA) activation (Fig. 2j). EP_2 or EP_4 inhibitors (EP_2i and EP_4i, respectively) significantly decreased PGE_2-induced, but not fsk-induced, activation of pCREB, supporting the receptor-mediated effects of PGE_2 on PKA (Fig. 2j). Similarly, addition of EP_2i or EP_4i antagonists restored production of IFNγ and TNF secretion following inhibition by PGE_2 but not in response to fsk (Fig. 2k). Interestingly, the addition of EP_2 and EP_4 antagonists together more significantly reduced PGE_2-mediated IFNγ and TNF inhibition than each antagonist alone, suggesting that concomitant blockade of $G\alpha_s$ activation by multiple $G\alpha_s$ receptors may afford better rescue from immune-suppressive effects on $CD8^+$ T cells. Next, we sought to determine whether inhibitory effects by PGE_2/cAMP-induced inhibition could be rescued by activation of an endogenously expressed $G\alpha_i$–GPCR CXCR3 with its ligand CXCL10. Although CXCL10 alone did not significantly affect IFNγ and TNF secretion, the addition of CXCL10 with PGE_2 alleviated inhibition by PGE_2 (Extended Data Fig. 2e). Together, these data strongly suggest that $G\alpha_s$ activation leads to dampening of $CD8^+$ T cell function, which can be rescued by either blocking $G\alpha_s$–GPCRs or by stimulating the $G\alpha_i$ axis.

To begin exploring the role of the $G\alpha_s$–PKA axis in PGE_2-mediated inhibition of T cell function, we generated conditional CD8-specific *Gnas*-knockout (KO) mice (Fig. 2l). We used mice with $CD8^+$ T cell-restricted Cre recombinase temporally controlled with tamoxifen[23] (*E8i-Cre*^{ERT2}) crossed with mice with *loxP* sites flanking *Gnas* exon 1 (referred to as CD8-*Gnas* KO; Fig. 2l and Supplementary Table 4). *E8i-Cre*^{ERT2} mice express the reporter gene in mature $CD8^+$ T cells but not in $CD4^+$ T cells, B cells, myeloid cells, dendritic cells or natural killer (NK) cell populations[24]. $CD8^+$ T cells were isolated and chronically stimulated following administration of tamoxifen. As expected, $CD8^+$ T cells with functional $G\alpha_s$ expressed less IFNγ and TNF after treatment with PGE_2 (Fig. 2m), but this inhibition was rescued in CD8-*Gnas* KO mice (Fig. 2m). In search of the potential mechanisms, we examined the involvement of PKA, a key downstream signaling effector of $G\alpha_s$. For these studies, we leveraged our protein kinase inhibitor (PKI) peptide mouse model[25]. *Tet-GFP-PKI* mice were crossed with *E8i*^{CreERT2}-*ROSA26*^{LSL}*rtTA* mice to generate a conditional, tetracycline-inducible PKI system to specifically inhibit PKA in $CD8^+$ T cells (referred to as CD8-*PKI*; Extended Data Fig. 3a–c and Supplementary Table 5). $CD8^+$ T cells were isolated from the CD8-*PKI* mice following tamoxifen and doxycycline administration and were chronically stimulated as described above. When green fluorescent protein (GFP)–PKI was expressed in chronically activated $CD8^+$ T cells, it prevented the decrease in IFNγ^+TNF$^+$ double-positive $CD8^+$ T cells caused by PGE_2 (Extended Data Fig. 3d), which mirrors *Gnas* deletion (Fig. 2m). This strongly suggests that *Gnas* and its downstream signaling target, PKA, are necessary for PGE_2-mediated inhibitory effects on $CD8^+$ T cells.

A chemogenetic model reveals immunosuppressive $G\alpha_s$ signaling

The use of designer receptors exclusively activated by designer drugs (DREADDs), which are GPCRs engineered to be non-responsive to endogenous ligands but responsive to the designer drug clozapine-*N*-oxide, can be exploited to achieve G-protein activation in a tissue-specific fashion[26]. To bypass potential off-target effects elicited by clozapine-*N*-oxide, we used the recently developed deschloroclozapine (DCZ), which affords higher affinity and more selective agonist activity for DREADDs[27]. To specifically interrogate the function of the $G\alpha_s$ signaling axis in $CD8^+$ T cells, we expressed $G\alpha_s$–DREADD by crossing *E8i*^{CreERT2} with *ROSA26*^{LSLGsDREADD} mice (Fig. 3a, Extended Data Fig. 4a and Supplementary Table 6). The resulting mice, referred to as CD8-GsD mice, were dosed with tamoxifen every day for 3 d, and $G\alpha_s$–DREADD expression and activation was subsequently verified (Fig. 3b). As assessed by quantitative PCR (qPCR), only in mice treated with tamoxifen was there demonstrable expression of $G\alpha_s$–DREADD in $CD8^+$ T cells and not in $CD4^+$ T cells (Fig. 3c). This confirmed tamoxifen-inducible recombination by the Cre recombinase for CD8-restricted $G\alpha_s$–DREADD expression.

To confirm activation of $G\alpha_s$–DREADD, mice were first dosed with tamoxifen, and then 0.01 mg per kg (body weight) DCZ was administered intraperitoneally (i.p.; Fig. 3b). After administration of tamoxifen and DCZ, mice were subsequently bled to assess pCREB induction by flow cytometry. Whereas the frequencies of pCREB$^+$NK1.1$^+$ NK cells, pCREB$^+$CD11b$^+$ myeloid cells and pCREB$^+$CD4$^+$ T cells were low and did not differ between DCZ-treated and untreated mice, the frequency of pCREB$^+$CD8$^+$ cells significantly

increased in DCZ-treated mice (Fig. 3d). Mice treated with DCZ did not show significant changes in frequency of $CD8^+$ or $CD4^+$ T cells, NK cells or $CD11b^+$ myeloid cells in the peripheral blood (Extended Data Fig. 4b). When we isolated peripheral blood from mice dosed with tamoxifen, the addition of DCZ in vitro also increased pCREB exclusively in $CD8^+$ T cells (Fig. 3e). These results confirm tamoxifen-inducible CD8-specific expression and activation of $G\alpha_s$–DREADD by DCZ in CD8-GsD mice. In agreement with our data for $G\alpha_s$–GPCR ligands, only in mice with tamoxifen-induced expression of $G\alpha_s$–DREADD did CD8–$G\alpha_s$ activation lead to significant decreases in IFNγ, TNF, Ki-67 and granzyme B concomitant with increases in PD-1 and TIM-3 expression (Fig. 3f–h and Extended Data Fig. 4c). To gain an understanding of downstream transcriptional modulations stimulated by $G\alpha_s$ signaling in $CD8^+$ T cells, we assessed gene expression of dual-specificity phosphatase 1 (*Dusp1*), a CREB target shown to negatively regulate T cell activation and function through inactivation of JNK and reduced NFATc1 (refs. 28,29; Fig. 3i). Stimulation of $G\alpha_s$–DREADD significantly increased the expression of *Dusp1*, in addition to *Tigit* and *Tox*, both of which are highly expressed on terminally exhausted $CD8^+$ T cells[30,31] (Fig. 3j). Together, activation of $G\alpha_s$–DREADD on $CD8^+$ T cells was sufficient to exacerbate exhaustion-related phenotypes, as indicated by decreased cytotoxic function in tandem with increased expression of exhaustion-related genes.

To assess biological relevance of the inhibitory $G\alpha_s$ signaling in $CD8^+$ T cells in the tumor setting, we used the OVA tumor model system to investigate the effect of $G\alpha_s$ signaling on recruitment and function of antigen-specific $CD8^+$ T cells. To study native T cell trafficking and function, we took advantage of an orthotopic head and neck cancer syngeneic mouse model, 4MOSC1, which recapitulates human head and neck cancer mutational signatures with ~93% similarity[32]. CD8-GsD or littermate control mice were given three doses of tamoxifen before tumor implantation with 4MOSC1-OVA, and DCZ was given every day starting 1 d after tumor implantation (Fig. 3k). CD8-GsD mice dosed with tamoxifen and with or without DCZ were killed at an early time point to quantify tumor-infiltrating SIINFEKL-tetramer$^+$$CD8^+$ T cells. There was a significant decrease in antigen-specific $CD8^+$ T cells infiltrating the tumor, and IFNγ and TNF from the bulk $CD8^+$ T cell population were both significantly decreased in DCZ-treated mice compared to in untreated mice (Fig. 3l,m). Our in vitro and in vivo data collectively indicate sufficiency of $G\alpha_s$ activation to drive exhaustion-related phenotypes and prevent trafficking of tumor-specific $CD8^+$ T cells.

$G\alpha_s$ signaling promotes $CD8^+$ T cell dysfunction and immunotherapy failure

We next investigated the effect of CD8-specific $G\alpha_s$ signaling on immunotherapy response and tumor killing in vivo. CD8-GsD mice were dosed with tamoxifen, and on day 0, 4MOSC1 cells or MC38-OVA cells were implanted into the tongues or flanks of mice, respectively (Fig. 4a). DCZ (0.01 mg per kg (body weight)) was administered daily to mice starting 1 d after tumor implantation. In the absence of agonist stimulation CD8-GsD mice with 4MOSC1 partially responded to anti-PD-1, similar to wild-type (WT) mice, as previously reported[32]; but activation of $G\alpha_s$-–DREADD by DCZ administration abolished any antitumoral responses (Fig. 4b). Additionally, although anti-PD-1 afforded a survival advantage in tumor-bearing mice, activation of the $G\alpha_s$ signaling axis in $CD8^+$ T cells led to

survival rates not significantly different from untreated mice (Fig. 4c). As controls, neither DCZ nor tamoxifen affected tumor growth in littermate control mice (Extended Data Fig. 5).

These findings prompted us to determine whether activation of $G\alpha_s$ signaling in $CD8^+$ T cells was sufficient to limit the long-term antitumor immunity from combined PD-1 and CTLA-4 ICB[32]. In the absence of DREADD ligand stimulation, 90% of CD8–$G\alpha_s$–DREADD mice responded to dual ICB with durable tumor regression (Fig. 4b,c). This was abrogated by the administration of DCZ (Fig. 4b,c and Extended Data Fig. 6), indicating that activation of the $G\alpha_s$ signaling axis on $CD8^+$ T cells is sufficient to limit T cell responses to ICB. Intriguingly, this was paralleled by a significant decrease of tumor growth in CD8-*Gnas* KO mice compared to in littermate control mice (Extended Data Fig. 7a). In these mice, there was a significant decrease in $CD8^+$ T cell exhaustion markers, such as $PD\text{-}1^+TIGIT^+$ tumor-infiltrating and experienced $CD8^+$ T cells lacking *Gnas* (Extended Data Fig. 7b,c).

Next, we determined whether diminished response to immunotherapies following activation of $G\alpha_s$ signaling was associated with diminished T cell functionality. Similar to our observations in the 4MOSC1 model, anti-PD-1 provided significant antitumor activity in CD8-GsD mice with MC38-OVA tumor cells in the absence of stimulation, but DCZ-treated mice led to failed responsiveness and worse overall survival (Fig. 4d,e). Treatment with anti-PD-1 in CD8-GsD mice led to a significant increase in $tetramer^+CD8^+$ T cells and IFNγ and granzyme B secretion (Fig. 4f), which were abolished by DCZ treatment concurrent with anti-PD-1 (Fig. 4f). These data suggest that activation of $G\alpha_s$ signaling exclusively on $CD8^+$ T cells leads to functional impairment and decreased recruitment of antigen-specific $CD8^+$ T cells at the tumor, which ultimately leads to failure to respond to immunotherapies.

$G\alpha_s$ signaling and reduced response to ICB therapy in humans

To begin exploring the clinical relevance of $G\alpha_s$–GPCR expression, we first investigated the correlation of expression between PD-1 and various $G\alpha_s$–GPCRs. In the The Cancer Genome Atlas skin cutaneous melanoma cohort, we found that expression of the GPCR genes *GPR65*, *PTGER2*, *PTGER4*, *ADRB2* and *ADORA2A* were all significantly positively correlated with PD-1 expression in bulk tumors (Fig. 5a). This suggests that PD-1 expression is likely concurrent with the expression of these GPCRs. We next asked whether the expression of these GPCRs could predict immunotherapy response. We analyzed a cohort of 32 individuals with metastatic melanoma (total of 48 biopsies) treated with anti-PD-1, anti-CTLA-4 or combination therapy and where scRNA-seq was performed on the tumors before and after therapy[33]. We observed that the expression levels of *GPR65*, *PTGER2*, *PTGER4*, *ADRB2* and *ADORA2A* align with those of non-responders to immunotherapy, and the expression of *PTGER2* and *ADORA2A* was significantly higher in $CD8^+$ T cells from non-responders than in those from responders, with *GPR65* nearing significance (Fig. 5b,c). We found that four of five of these $G\alpha_s$–GPCRs (*PTGER4*, *GPR65*, *ADORA2A* and *PTGER2*) have significant predictive power to identify individuals with melanoma who would not respond to immunotherapy. In this analysis, *PTGER2* ranked at the top, with the highest area under the curve (AUC) of 0.78 (Fig. 5c). To test the extent of the role of immune suppression in immunotherapy response by $G\alpha_s$–GPCR pathway across cancers,

we next computed the correlation between mean $G\alpha_s$–GPCR pathway levels in a cancer type and immunotherapy objective response rate (ORR) observed across 16 cancer types[14,34,35]. Remarkably, in agreement with our hypothesis, we found that the mean $G\alpha_s$–GPCR pathway levels in a cancer type are most negatively correlated with the immunotherapy ORR out of all the G-protein signaling programs (Fig. 5d).

In summary, we propose a $G\alpha_s$–GPCR signaling axis that, when activated in $CD8^+$ T cells, is sufficient to decrease cytotoxic function, exacerbate exhaustion-related phenotypes and abolish responses to immunotherapy (Fig. 6). Thus, the concomitant blockade of $G\alpha_s$–GPCRs with other inhibitory receptors, including PD-1 and CTLA-4, may be needed to garner a more effective and durable response to immunotherapy.

Discussion

Numerous recent studies have investigated the expression profiles of intratumoral T cells at singe-cell resolution, revealing gene expression programs characterizing each individual T cell population and their functional consequences[36]. While we have not validated these findings individually, we have developed computational pipelines enabling the integration of these scRNA-seq datasets from hundreds of thousands of intratumoral immune cells and transcriptomic information delineating response to ICB. By combining this wealth of information with the development of a chemogenetic approach to stimulate CD8-restricted $G\alpha_s$–GPCRs, we have now uncovered a $CD8^+$ T cell GPCR–$G\alpha_s$ signaling axis promoting T cell dysfunction and immunotherapy failure.

GPCR signaling networks in the TME orchestrate anticancer immune defense mechanisms, as demonstrated by chemokines and chemokine receptors displayed on both antitumoral and protumoral immune cells[8]. However, metabolites and inflammatory mediators accumulating in the TME can bind GPCRs that exert immunosuppressive effects. These include the nucleoside adenosine, a product from the breakdown of ATP by ectonucleotidases CD39 and CD73, and the inflammatory mediator PGE_2, which is enzymatically derived from the cyclooxygenase (COX) isoforms COX1 and COX2, which are upregulated in most solid cancers[37]. Both adenosine and PGE_2 stimulate GPCRs expressed in many immune cell types and exert their immunosuppressive activity by acting primarily on $G\alpha_s$-coupled receptors, $A_{2A}R$ (*ADORA2A*) and EP_2 (*PTGER2*) and EP_4 (*PTGER4*), respectively[12,13]. Stimulation of $A_{2A}R$ provides a broad immunosuppressive signal through multiple cell types, including T cells, NK cells, dendritic cells and neutrophils[13], and blocking antibodies to CD73 and CD39 are under current evaluation for combination with ICB[13]. PGE_2 has been linked to recruitment of myeloid-derived suppressor cells and decreased $CD8^+$ T cell activation and NK cell recruitment, among others[8,38]. Hence, nonsteroidal anti-inflammatory drugs that block COX2 and/or COX1 and COX2 and EP receptors represent promising targets for combination with ICB[39]. However, the precise role of these GPCRs in $CD8^+$ T cell function is much less understood, as most studies have relied on global gene KO strategies and systemic inhibition of receptors or biosynthetic pathways involved in ligand production. This may limit the ability to define key regulated events in $CD8^+$ T cells and overlook the existence of redundant or compensatory mechanisms that may render therapeutic interventions blocking these GPCRs ineffective.

Given the complexity of receptor expression in multiple immune and tumor cells in the TME and difficulty of unraveling the function of these $G\alpha_s$-linked GPCRs in $CD8^+$ T cells, we took a synthetic biology approach to build chemogenetic DREADDs and gain spatial and temporal control of $G\alpha_s$ signaling specifically in $CD8^+$ T cells. The uniqueness of the CD8-GsD mouse model afforded us the opportunity to interrogate functions of $G\alpha_s$–cAMP–PKA irrespective of the GPCR that provides the activation. We found that activation of $G\alpha_s$-linked GPCRs in $CD8^+$ T cells is sufficient to limit antigen-specific $CD8^+$ T cell recruitment, abolish cytotoxic function and abrogate the antitumor responses to both anti-PD-1 and anti-CTLA-4. $G\alpha_s$ stimulation also augmented expression of terminal exhaustion-related receptors, such as PD-1 and TIM-3. Indeed, our studies using the chemogenetic $G\alpha_s$–DREADD, $G\alpha_s$ KO and PKA inhibition models all link the CD8–$G\alpha_s$–PKA axis to T cell dysfunction in effector $CD8^+$ T cells and tumor-infiltrating $CD8^+$ T cells.

Although the underlying mechanisms by which $G\alpha_s$–PKA may exert these inhibitory functions are yet to be fully elucidated, it is likely that in the TME, $G\alpha_s$–PKA can directly inhibit T cell migration and contribute to the expression of $CD8^+$ T cell exhaustion programs. In turn, the implication of $G\alpha_s$-linked GPCRs as negative regulators and the heightening of $CD8^+$ T cell dysfunction in the TME provide a strong foundation for the future exploration of the GPCR–$G\alpha_s$–PKA axis for the development of precision cancer immunotherapy in combination with ICB. In this regard, although the abundance of ligands in the TME and GPCR expression on tumor-infiltrating $CD8^+$ T cells is likely tumor-type specific, our pan-cancer computational analysis provides a shared landscape of GPCRs broadly associated with intratumoral exhausted $CD8^+$ T cells, which includes *ADORA2A*, *PTGER2*, *PTGER4*, *ADRB1*, *ADRB2* and *GPR65*, all of which converge to the initiation of $CD8^+$ T cell exhaustion programs by the activation of the $G\alpha_s$–PKA pathway (Fig. 6). This may have a direct clinical impact, as it may provide a rationale for the use of readily available β-adrenergic blockers, such as propranolol, in individuals with cancer with elevated circulating adrenaline/noradrenaline, which are typical of physical and emotional stress conditions, in lesions exhibiting *ADRB1* or *ADRB2* expression in intratumoral $CD8^+$ T cells[40]. Intriguingly, GPR65, a proton-sensing GPCR, also emerged as a $G\alpha_s$–GPCR significantly correlated with T cell dysfunction. Hypoxia and acidosis resulting from enhanced anaerobic metabolism, referred to as the ‘Warburg effect’, is a hallmark of most solid tumors[41] and has been associated with immune exclusion. Therefore, expression of GPR65 on $CD8^+$ T cells may provide a mechanism of intrinsic resistance to cytotoxic $CD8^+$ T cells, which can be disrupted, for example, by the future development of GPR65 inhibitors. Another unexpected finding from our study is that all of the $G\alpha_s$–GPCRs that we identified as part of our pan-cancer analysis were significantly correlated with *PDCD1* (PD-1) expression, and five of the six $G\alpha_s$–GPCRs that we analyzed had significant predictive power to predict responses to immunotherapy in individuals with melanoma. Thus, our studies may provide a valuable resource for the future development and exploration of targeting $CD8^+$ T cell-specific GPCRs as part of combination immunotherapies.

Our data also suggest that many $G\alpha_s$–GPCRs expressed on $CD8^+$ T cells may be functionally redundant, which raises the question of whether to target individual receptors based on the specific expression profile of each individual or simultaneously. As an

alternative approach, perhaps targeting the shared downstream mechanisms, specifically cAMP–PKA, may provide a more feasible approach to targeting the $G\alpha_s$ immune checkpoint, thus circumventing the emerging receptor–ligand redundancy. As the prospect of cancer immunotherapies will likely rely on combinatorial strategies blocking additional targets, studies interrogating downstream signaling mechanisms of T cell dysfunction and exhaustion will become important for uncovering these targets. Our work here investigating the pan-cancer GPCR repertoire of tumor-infiltrating $CD8^+$ T cells combined with the use of synthetic biology approaches to reveal the specific immune-suppressive functions of $G\alpha_s$ signaling in $CD8^+$ T cells can now provide opportunities to achieve multitargeted $G\alpha_s$–GPCR inhibition or $G\alpha_s$–cAMP–PKA pathway modulation with the overall goal of enhancing responses to immunotherapies.

Methods

Study design

The sample size for each experiment was selected based on historical data and previous publications using the same tumor models[32,42]. Mice from in vivo experiments were randomized based on tumor volume before initiation of treatment or data collection. Data collection and analysis were not performed blind to the conditions of the experiments. Data reported for all experiments were not subjective but rather based on quantitative analyses. All data collected were included and represented in the main figures or supplementary materials.

Cell lines, antibodies and other reagents

The 4MOSC1 cell lines were previously generated in-house by our lab. The MC38 cell line was generously gifted by A. Sharabi (University of California, San Diego). The MC38-OVA cell line was generated by retroviral transduction with pMSCV-OVA (gift from A. Sharabi). The 4MOSC1-SIINFEKL cell line was generated by lentiviral transduction with the pLenti-CMV GFP DEST vector. The 4MOSC1 cell lines were grown in keratinocyte medium with growth supplement, cholera toxin, epidermal growth factor and antibiotics. MC38-OVA cells were grown in DMEM supplemented with 10% fetal bovine serum, 1% antibiotics/anti-mycotics and 1 μg ml^{-1} blasticidin. All cell lines were grown at 37 °C and 5% CO_2. PD-1 antibody (clone J43, BE0033-2; clone RMP1-14, BE0146), CTLA-4 antibody (clone 9H10, BP0131), isotype antibody (Armenian hamster IgG isotype control, BE0091; rat IgG isotype control, BE0251; Syrian hamster IgG isotype control, BE0087) and CD8 depletion antibody (clone YTS 169.4, BE0117) were obtained from Bio X Cell. DCZ was purchased from Tocris (7193).

Mice

All animal experiments used in this study were approved by the Institutional Animal Care and Use Committee (IACUC) of the University of California, San Diego, with protocol ASP S15195. Mice at Moores Cancer Center, University of California, San Diego, were housed in a microisolator and individually ventilated cages supplied with acidified water and were fed 5053 irradiated Picolab rodent diet 20 from LabDiet. Temperature for laboratory mice in our facility is mandated to be between ~18 and 23 °C with 40–60% humidity, and a 12-h

light/12-h dark cycle was maintained for the facility. All animal manipulation activities were conducted in laminar flow hoods. All personnel are required to wear scrubs and/or a lab coat, mask, hair net, dedicated shoes and disposable gloves after entering the animal rooms. All animal studies conducted in this study were approved by the IACUC of the University of California, San Diego, with protocol ASP S15195.

The *E8I*^{CreERT2} mice were obtained from D. Vignali (University of Pittsburgh)[23].The *Gnas*-exon 1$^{fl/fl}$ mice were obtained from R. Iglesias-Bartolome (National Institutes of Health)[25]. CD8-*Gnas* KO mice were generated by crossing *E8I*^{CreERT2} with *Gnas*-exon 1$^{fl/fl}$ mice. Information regarding genotyping of CD8-*Gnas* KO mice is listed in Supplementary Table 4. The Tet-GFP-PKI mice were obtained from R. Iglesias-Bartolome (National Institutes of Health). Transgenic mice were generated as previously described using a codon-optimized sequence for the 1–24 amino acids from PKIA fused to GFP[25]. The *ROSA26*$^{tTA\text{-}IRES\text{-}EGFP}$ mice were obtained from A. Nagy (Samuel Lunenfeld Research Institute)[43]. Information regarding genotyping of CD8-PKI mice is listed in Supplementary Table 5. OT-1 mice (C57BL/6-Tg(*TcraTcrb*)1100Mjb/J, 003831) were purchased from the Jackson Laboratory and bred in-house. The *ROSA26*^{LSLGsDREADD} mice were obtained from R. Berdeaux (The University of Texas, Houston)[44]. *ROSA26*^{GsDREADD} mice were generated by crossing *E8I*^{CreERT2} mice with *ROSA26*^{LSLGsDREADD} mice. Information regarding genotyping of CD8-GsD mice is listed in Supplementary Table 6.

Tamoxifen, doxycycline and DCZ treatment

Tamoxifen was purchased from Sigma-Aldrich. Where indicated, CD8-GsD mice were dosed with tamoxifen at 75 mg per kg (body weight). A stock solution of 15 mg ml^{-1} was prepared by dissolving 75 mg of tamoxifen in 5 ml of miglyol and dissolved at 37 °C. After dissolving, the solution was stored at −20 °C protected from light. Mice were given 1.5 mg in 100 μl by i.p. injection for 3 d consecutively before tumor implantation or cell isolation. Mice were delivered 25 mg per kg (body weight) doxycycline in the diet (Bio-Serv) beginning the same day as initial tamoxifen administration. Mice consumed doxycycline for 5 d consecutively before cell isolation. DCZ was purchased from Tocris. Mice were dosed with DCZ at 0.01 mg per kg (body weight). A stock solution of 10 mg ml^{-1} was prepared by dissolving 10 mg of DCZ into 1 ml of DMSO. Subsequently, a working concentration of 0.002 mg ml^{-1} DCZ in PBS was prepared, and mice were given 0.0002 mg of DCZ in 100 μl i.p. daily.

In vivo mouse tumor models

For 4MOSC1 and 4MSOC1-SIINFEKL tumor xenografts, WT female C57BL/6 mice (4–6 weeks old) were purchased from Charles River Laboratories. WT mice or age-matched CD8-GsD mice were first given tamoxifen i.p. every day for 3 d. On the fourth day, 5 × 10^5 tumor cells were injected into the tongues of mice, and when tumors reached ~30 mm^3 (4–5 d after implantation), mice were treated by i.p. injection with isotype control antibody, anti-PD-1 (clone J43) or anti-CTLA-4 (clone 9H10; i.p. 10 mg per kg (body weight) three times a week). Where indicated, DCZ (i.p. 0.1 mg per kg (body weight)) was started on the fifth day and given daily.

For MC38-OVA tumor xenograft studies, WT female C57BL/6 mice (4–6 weeks old) were purchased from Charles River Laboratories. WT mice or age-matched CD8-GsD mice were first given tamoxifen i.p. every day for 3 d. On the fourth day, 1×10^5 cells were injected subcutaneously into the flanks of mice. When tumors reached ~100 mm^3 (8–10 d after implantation), mice were treated by i.p. injection with either isotype control antibody or anti-PD-1 (clone RMP1-14; i.p. 10 mg per kg (body weight) three times a week). Where indicated, DCZ treatment was started on the fifth day and given daily.

All mice were killed after the completion of the treatment, when control-treated mice succumbed to tumor burden or when tumors ulcerated. Mice were also killed when tongue tumors reached 8 mm in diameter or when flank tumors reached 1,500 mm^3, as determined by the ASP guidelines.

Tumors were dissected as previously described[42]. In brief, tumors were isolated, minced and resuspended into a tumor dissociation kit (Miltenyi Biotec) and were processed with the gentleMACS Octo dissociator, according to the manufacturer's protocol for tumor dissociation. Digested tumors were then passed through 70-μm strainers to generate single-cell suspensions and were processed further for flow cytometric analysis.

In vitro T cell cultures and isolations

Splenocytes were isolated from 4- to 6-week-old mice and were mechanically disrupted. Red blood cells were lysed in red blood cell lysis buffer (BioLegend) according to manufacturer's instructions. $CD8^+$ T cells were isolated with an EasySep CD8 isolation kit by negative selection. For determining the expression of transgenes in $CD4^+$ or $CD8^+$ T cells, $CD8^+$ T cells were first isolated through positive selection with CD8a MicroBeads (Miltenyi Biotec), followed by positive selection of the prior eluted fraction with CD4 MicroBeads. For activation, cells were then cultured at 1×10^6 cells per well in 1 ml in 24-well plates with Dynabeads Mouse T-Activator CD3/CD28 beads at a 1:1 cell:bead ratio with 25 U ml^{-1} human IL-2 (hIL-2; PeproTech) for 48 h. Naive $CD8^+$ T cells were cultured with 25 U ml^{-1} hIL-2 alone. After 48 h, activated cells were collected, counted and split into the 'acute' or 'chronic' activation groups. For acute activation, $CD8^+$ T cells were cultured at 5×10^4 cells per well in 200 μl in 96-well round-bottom plates with 25 U ml^{-1} hIL-2 without beads. For chronic activation, $CD8^+$ T cells were cultured at the same cell density with 25 U ml^{-1} hIL-2 and with CD3/CD28 beads at a 1:2.5 cell:bead ratio. Where indicated, GPCR agonists were added at the following concentrations: 1 μM 16,16-dimethyl PGE_2 (Tocris), 5 μM dobutamine hydrochloride (Tocris) and 5 μM CGS-21680 hydrochloride (Tocris). For PGE_2 experiments, where indicated, inhibitors or CXCL10 were added at the following concentrations: 1 μM fsk (Tocris), 1 μM PF 04418948 (EP_2i; Tocris), 1 μM ONO AE3 208 (EP_4i; Tocris), 10 nM CXCL10 (gifted by T. Handel, University of California San Diego, La Jolla); PGE_2 and inhibitors were added in the last 24 h of culture. Inhibitors were first added for 30 min, and then 1 μM PGE_2 was added in the last 24 h of culture. For CD8-GsD in vitro experiments, 2 μM 4-hydroxytamoxifen (Sigma-Aldrich) was included in culture. Additionally, DCZ was added at a concentration of 0.002 mg ml^{-1}.

In vitro coculture tumor killing assay

Splenocytes were isolated from OT-1 mice (4–6 weeks old) and activated with 100 nM OVA peptide (257–264; GenScript) and 50 U ml^{-1} hIL-2 (PeproTech) for 48 h. After 48 h, fresh medium with 50 U ml^{-1} IL-2 was added to the culture and incubated for an additional 24 h. Cells were then collected, replated and expanded at 1×10^6 cells per ml.

For the specific cytotoxicity assay, tumor cells (target) were plated at 50,000 cells per well in a 24-well plate. OT-1 T cells (effector) were then added at a 1:5 target:effector ratio. Where indicated, GPCR agonists were added at the following concentrations: 1 μM 16,16-dimethyl PGE_2 (Tocris), 5 μM dobutamine hydrochloride (Tocris) and 5 μM CGS-21680 hydrochloride (Tocris). The coculture was left for 36 h, and cell viability was assessed by flow cytometric staining with Zombie Aqua viability dye (BioLegend).

Flow cytometry

The following flow cytometry antibodies (mouse) were purchased from BioLegend: CD45 (30-Fll; 1:100), CD3 (145-2Cll; 1:200), CD8a (53–6.7; 1:200), PD-1 (29F.1A12; 1:100), TIM-3 (RMT3-23; 1:100), IFNγ (XMGl.2; 1:100), granzyme B (GBll; 1:100), TNF-α (MP6-XT22; 1:100), CTLA-4 (UC10-4B9; 1:100), LAG3 (C9B7W; 1:100) and Ki-67 (16A8; 1:100). Anti-CREB (pS133)/ATF-1 (pS63; 1:20) was purchased from BD Biosciences. For viability staining of $CD8^+$ T cells in vitro, cells were washed once with PBS and stained with Zombie Aqua viability dye (BioLegend) according to manufacturer's instructions. Cell surface staining was done for 30 min at 4 °C. For intracellular and transcription factor staining, cells were stimulated with 1× cell activation cocktail with brefeldin A (BioLegend) in medium for 4–6 h at 37 °C before viability staining. Unstimulated cells were used as a control. After cell surface staining, cells were fixed with a FOXP3/transcription factor buffer set and stained with intracellular antibodies for 45 min at room temperature.

For flow cytometry acquisition using the Agilent NovoCyte Advanteon, the voltage and photodetector gains were automatically determined by calibration and quality control of the instrument. Automatic compensation was then performed using single-stained samples of OneComp eBeads compensation beads (Thermo Fisher Scientific), and voltage parameters were automatically determined based on predetermined photodetector gains from the calibration. Optimal dilutions for antibodies used in this study were determined based on titrating the antibody amount and adjusting the cell number used. The gating strategy for flow cytometry experiments is shown in Extended Data Fig. 8a,b, and gates were drawn based on non-activated and unstimulated control cells.

Detection of pCREB

For CD8-GsD pCREB activation experiments in vivo, CD8-GsD mice were first given tamoxifen i.p. every day for 3 d. DCZ (i.p. 0.01 mg per kg (body weight)) was started on the fifth day and given daily for 5 d. Blood was collected from mice by retro-orbital bleeding, and samples were lysed and fixed with Lyse/Fix buffer (BD Biosciences). Cells were then permeabilized with Perm Buffer II (BD Biosciences) and stained with anti-CREB (pS133)/ATF-1 (pS63; BD Biosciences) according to the manufacturer's instructions.

For CD8-GsD pCREB activation experiments in vitro, CD8-GsD mice were first given tamoxifen i.p. every day for 3 d. On the fourth day, blood was collected from mice by retro-orbital bleeding. Red blood cells were lysed in red blood cell lysis buffer (BioLegend) according to manufacturer's instructions; 0.002 mg ml^{-1} DCZ was added to the cultures for 15 min, and cells were fixed with CytoFix buffer (BD Biosciences) according to manufacturer's instructions. Cells were then permeabilized with Perm Buffer II (BD Biosciences) and stained with extracellular antibodies and with anti-CREB (pS133)/ATF-1 (pS63; BD Biosciences) according to manufacturer's instructions.

For PGE_2 pCREB activation experiments in vitro, chronically activated $CD8^+$ T cells were serum starved for 1 h. PGE_2 (1 μM) was then added for 15 min in the presence or absence of inhibitors, and cells were fixed with CytoFix buffer (BD Biosciences) according to manufacturer's instructions. Cells were then permeabilized with Perm Buffer II (BD Biosciences) and stained with extracellular antibodies and with anti-CREB (pS133)/ATF-1 (pS63; BD Biosciences) according to manufacturer's instructions.

qPCR

RNA was extracted from naive $CD8^+$ T cells, activated $CD8^+$ T cells, chronically stimulated $CD8^+$ T cells and chronically stimulated $CD8^+$ T cells treated with DCZ with an RNeasy mini kit following manufacturer's instructions (Qiagen). RNA (100 ng) was converted to cDNA using a SuperScript VILO cDNA synthesis kit (Thermo Fisher Scientific). qPCR was performed using SYBR Select master mix (Thermo Fisher Scientific). *Actb* was used for normalization. The following primers were used for qPCR: *Dusp1* forward 5′-GTTGTTGGATTGTCGCTCCTT-3′; *Dusp1* reverse 5′-TTGGGCACGATATGCTCCAG-3′; *Tox* forward 5′-GCTCCCGTTCCATCCACAAA-3′; *Tox* reverse 5′-TCCCAATCTCT TGCATCACAGA-3′; *Tigit* forward 5′-GAATGGAACCTGAGGAGTCTCT-3′; *Tigit* reverse 5′-AGCAATGAAGCTCTCTAGGCT-3′; *Actb* forward 5′-GG CTGTATTCCCCTCCATCG-3′; *Actb* reverse 5′-CCAGTTGGTAACAA TGCCATGT-3′.

Bioinformatics analysis

For scRNA-seq integration, we used the Seurat scRNA-seq SCTransform integration method[45]. We collected 30 datasets with publicly available raw counts across 19 cancer types. Each dataset was transformed individually with the SCTransform function to regress out mitochondrial percentage, S score, G2M score and DIG score. The S, G2M and DIG scores were obtained from a recent publication. The data were then prepared for integration with the SelectIntegrationFeatures, Prep-SCTIntegration and FindIntegrationAnchors functions and integrated with the IntegrateData function. Principle-component analysis and dimensionality reduction were performed with the RunPCA and RunU-MAP functions, respectively. $CD8^+$ T cell states were identified using the ProjecTILs package, the multimodal reference mapping workflow in Seurat and key marker genes, resulting in five major functional states: naive, cytotoxic, effector memory, proliferative and exhausted. To examine the relative expression of GPCRs between $CD8^+$ T cell subtypes, the average expression of each GPCR was calculated for each of the five groups, row normalized for each GPCR and visualized on a circular heat map using circlize

v0.4.12 and ComplexHeatmap v2.6.2. The package versions used were circlize v0.4.12, ComplexHeatmap 2.6.2, ggplot2 3.3.3 and Seurat 4.0.1.

For calculation of the T cell dysfunction score, the average expression of all genes in the T cell dysfunction gene set was calculated and plotted for each $CD8^+$ T cell from the integrated $CD8^+$ T cell dataset. Spearman correlations for each GPCR and the dysfunction score were calculated by correlating expression of the GPCR with mean expression of the dysfunction gene set for each $CD8^+$ T cell from the melanoma dataset (GSE120575).

For differential expression analysis, three datasets of LCMV RNA-seq data were batch corrected with ComBat (v3). Subsequently, DESeq2 (version 1.32) was used to analyze all effector $CD8^+$ T cells versus all exhausted $CD8^+$ T cells. *P* values from this analysis were adjusted for multiple hypothesis correction and false discovery rates with Benjamini–Hochberg testing[46,47].

For gene set enrichment analysis, we created GPCR gene sets on the basis of their G-protein coupling mechanisms. We considered either G-protein family-level transduction mechanisms from IUPHAR or individual G-protein couplings from a recent experimental TGFα shedding assay that we augmented through machine learning-based predictions[22,48]. For each G-protein family coupling from IUPHAR, we created gene sets based on primary and secondary mechanisms either in isolation or combined. For the experimental TGFα shedding assay, we considered as couplings binding with log (relative intrinsic activity, RAi) values greater than −1.0. We defined the predicted couplings by considering either a looser (0.5) or more stringent (0.9) cutoff of the coupling probabilities outputted from PRECOG[48]. For each individual G-protein coupling, we created gene sets by considering the experimental and predicted couplings either in isolation or in combination. We created gene sets in the .gmt format by considering corresponding Entrez IDs, and we performed gene set enrichment analysis through ClusterProfiler (v.4.6.2)[49], giving as an input the list of genes ranked according to $\log_2$ (fold change) values from differential expression analysis.

For analysis of ORR, expression profiles of tumors from 2,277 individuals across 14 cancer types treated with immune check-point inhibitors were collected[14,35,50]. Mean expression of each GPCR was calculated and classified based on coupling information from IUPHAR.

Statistical analysis

Graphs were plotted using GraphPad Prism v9.2.0 (GraphPad Software) and R (v4.2.2). Where indicated, data are expressed as mean ± s.e.m. The following tests were performed (see figure legends for details): correlation, unpaired two-tailed Student's *t*-test, one- or two-way ANOVA and log-rank (Mantel–Cox) tests for Kaplan–Meier survival curves. Statistical significance was determined as $*P < 0.05$, $**P < 0.01$ and $***P < 0.001$. Data distribution was assumed to be normal, but this was not formally tested.

Extended Data

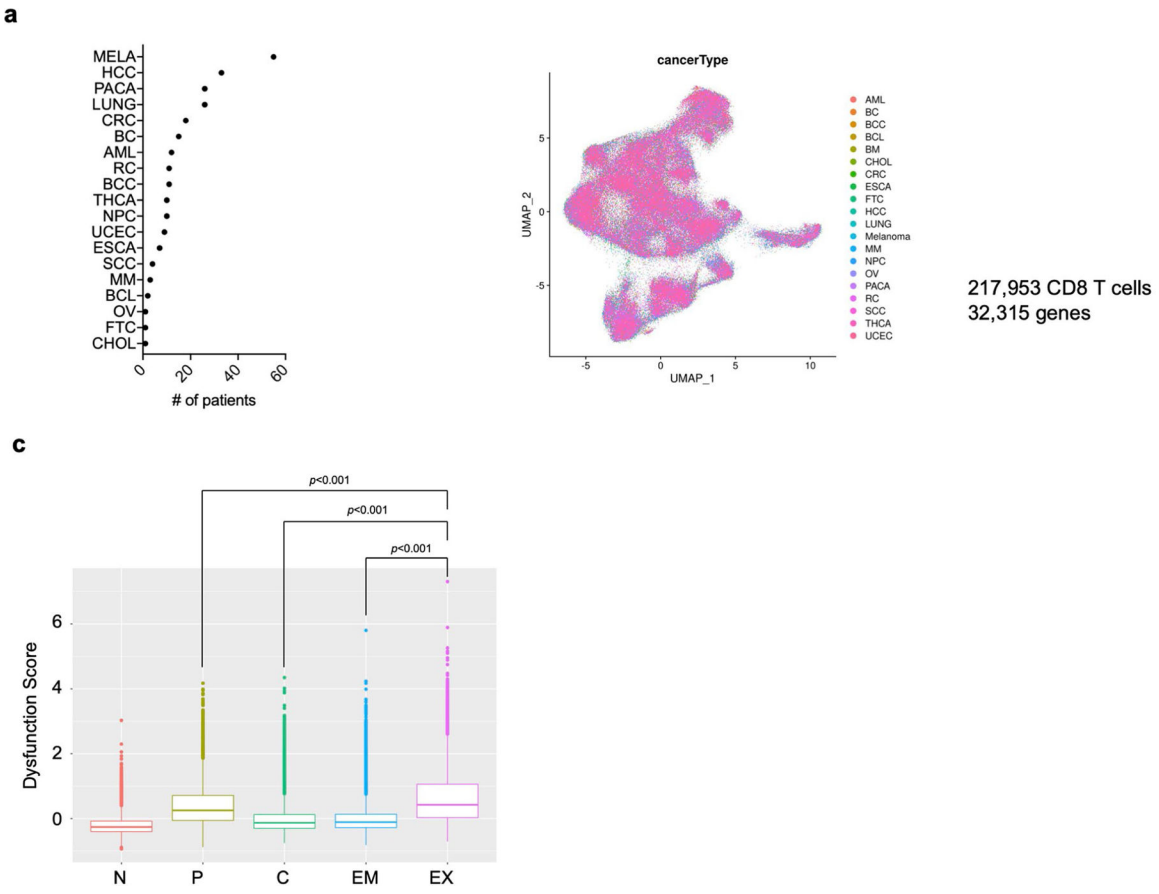

Extended Data Fig. 1 |. Patient and cancer information for integration analysis of CD8 T cells.
a, Information about patients, cancer type, and dataset used in the singe-cell RNA-seq integration. **b**, Visualization of 217,953 CD8 T cells after integration from 30 singe-cell RNA-seq datasets. **c**, Statistical comparison of calculated dysfunction score from tumor-infiltrating populations of CD8s characterized from Fig. 1b. Each dot represents one cell from groups listed in Supplementary Table 1a. Naïve: lower bound=0.147, middle bound=0.229, upper bound=0.337, 25th percentile=0.228, 75th percentile=0.231. Proliferating: lower bound=0.372, middle bound=0.564, upper bound=0.790, 25th percentile=0.556, 75th percentile=0.571. Cytotoxic: lower bound=0.184, middle bound=0.290, upper bound=0.447, 25th percentile=0.288, 75th percentile=0.292. Effector Memory: lower bound=0.209, middle bound=0.304, upper bound=0.431, 25th percentile=0.303, 75th percentile=0.305. Exhausted: lower bound=0.361, middle bound=0.555, upper bound=0.800, 25th percentile=0.551, 75th percentile=0.559.

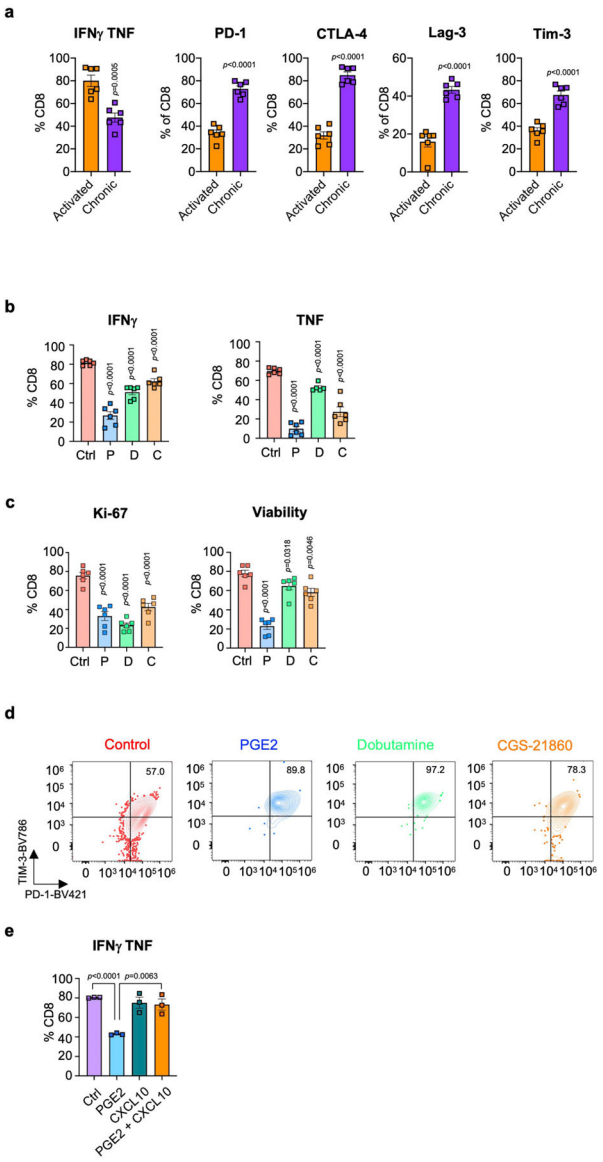

Extended Data Fig. 2 |. Effect of targeting the Gαs/PKA signaling pathway in CD8 T cells.
a, Upregulation of inhibitory receptors and decrease of IFNγ and TNF in chronically versus acutely simulated CD8 T cells. The average relative expression and s.e.m. are shown (n = 6 biologically independent samples). **b**, Significant decrease of IFNγ or TNF with $G\alpha_s$ agonists in chronically stimulated CD8 T cells. The average relative expression and s.e.m. are shown (n = 6 biologically independent samples). **c**, Significant decrease of Ki-67 and viability with $G\alpha_s$ agonists in chronically stimulated CD8 T cells. The average relative expression and s.e.m. are shown (n = 6 biologically independent samples). **d**, Representative flow cytometry plots showing expression of Tim-3 and PD-1 in chronically stimulated CD8 T cells after treatment with 1 μM PGE2 (P), 5 μM Dobutamine (D), or 5 μM CGS-21860 (C). **e**, Effect of CXCL10 on PGE2-mediated decrease in IFNγ and TNFα The average frequency and s.e.m. are shown (n = 3 per group). Statistical significance was determined

by two-way ANOVA. Unless indicated otherwise, statistical significance was determined by two-tailed unpaired Student's *t*-test.

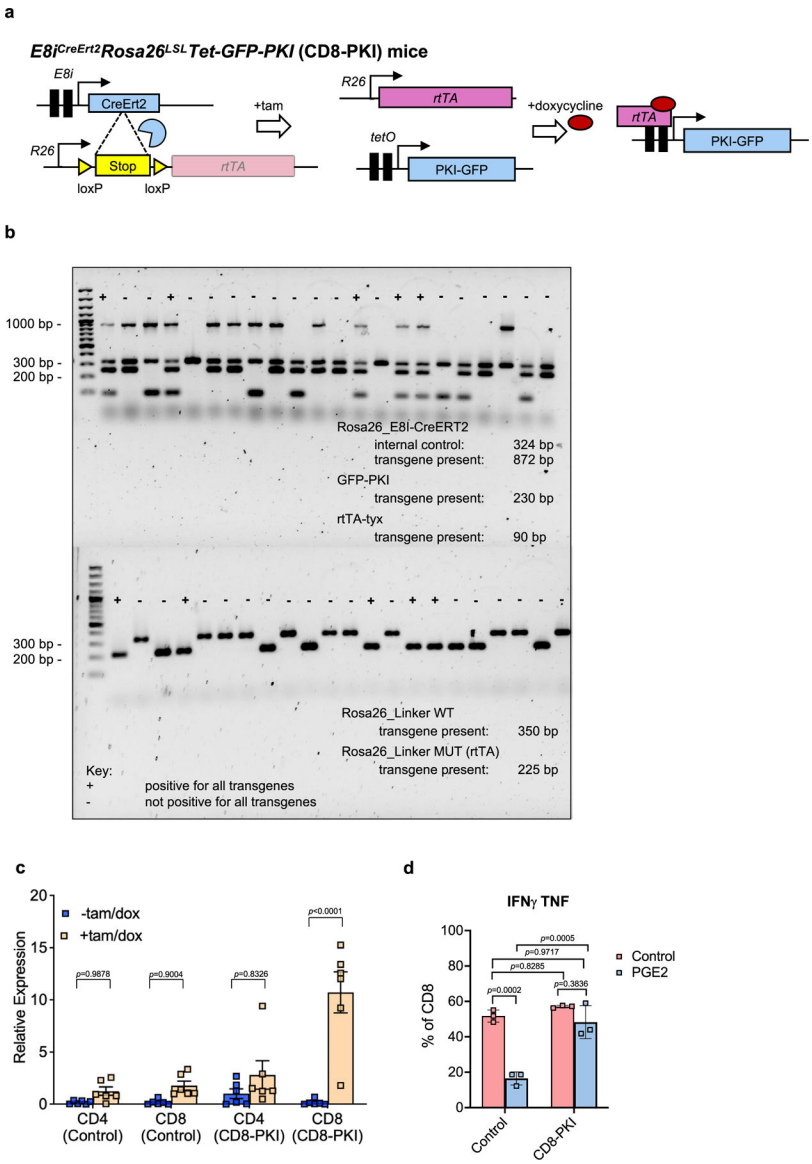

Extended Data Fig. 3 |. Development of a CD8-restricted PKI transgenic mouse model.
a, Scheme illustrating the generation of CD8-PKI mice. **b**, Genotyping information for CD8-PKI mice. **c**, Confirmation of PKI expression in CD4 or CD8 T cells isolated from splenocytes of CD8-PKI mice and littermate controls after induction by doxycycline and tamoxifen. The average relative expression and s.e.m. are shown (n = 6 mice per group). **d**, Quantification of IFN**γ** and TNF inhibition by PGE2 in chronically stimulated CD8 T cells from CD8-PKI mice. The average relative expression and s.e.m. are shown (n = 3 biologically independent samples). Statistical significance was determined by two-way ANOVA.

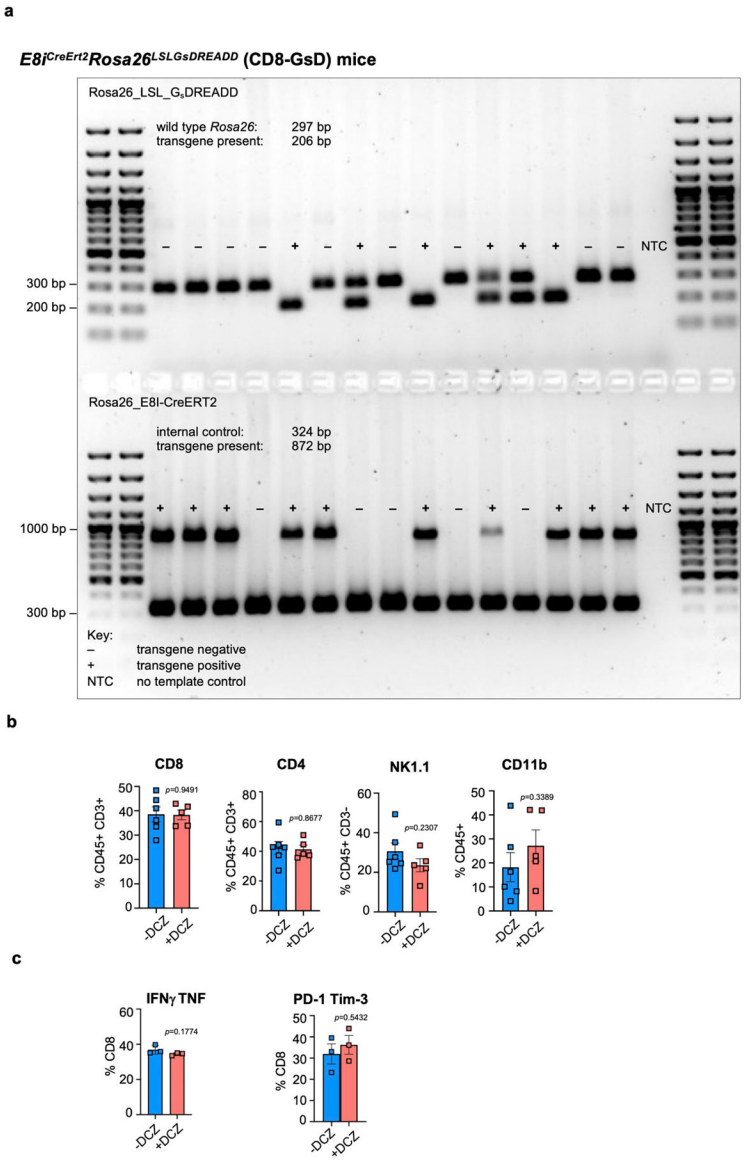

Extended Data Fig. 4 |. Development of a CD8-restricted Gαs-DREADD transgenic mouse model.

a, Genotyping confirmation for CD8-GsD mice. Primers detecting the *Gαs-DREADD*, *ROSA26*, and *E8i-Cre* were used to confirm recombination by the Cre-recombinase. Information about primers and genotyping is listed in Supplementary Table 4. **b**, Effect of DCZ on circulating CD8, CD4, NK cells, and CD11b myeloid cells in the peripheral blood of CD8− GsD mice treated with tamoxifen and 5 doses of DCZ (n = 5 mice for -DCZ; n = 6 mice for +DCZ). **c**, Effect of DCZ on non-tamoxifen-treated CD8-GsD mice. Quantification of IFNγ and TNF and PD-1 and Tim-3 in non-tamoxifen-treated CD8 T cells treated with or without DCZ. The average frequency and s.e.m. are shown (n = 3 biologically independent samples). Statistical significance was determined by two-tailed unpaired Student's *t*-test.

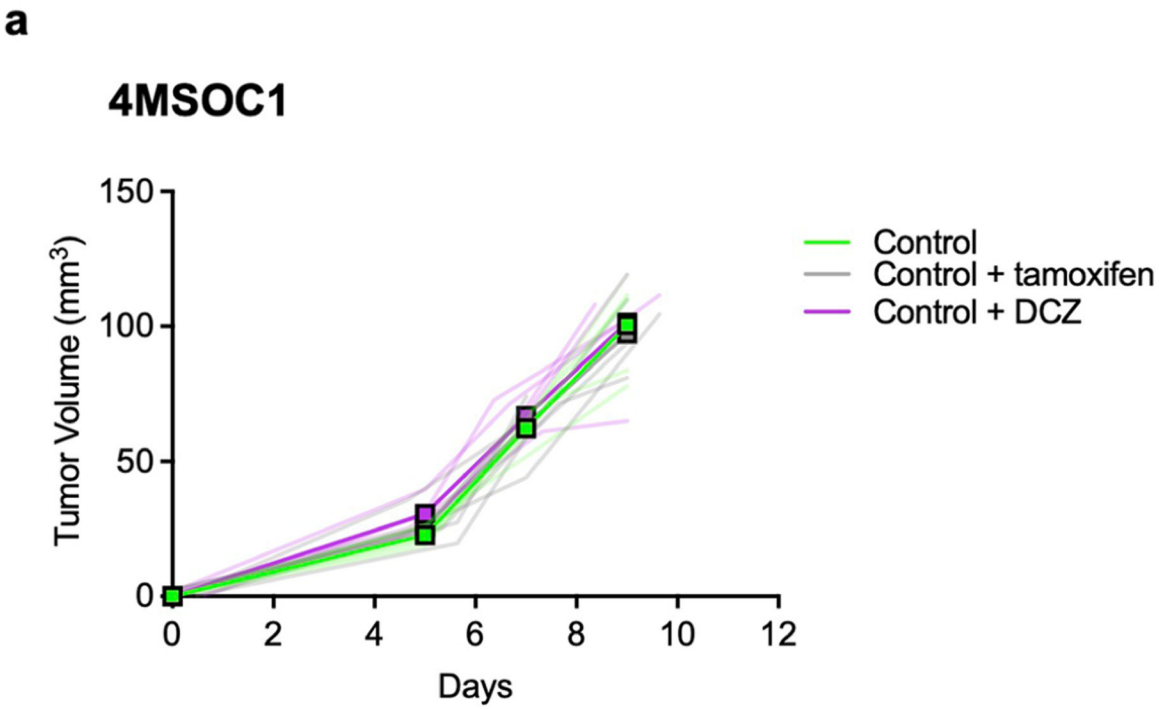

Extended Data Fig. 5 |. Effect of tamoxifen and DCZ on tumor growth.
Tumor growth curve of CD8-GsD littermate control mice implanted with 4MOSC1 tumors treated with or without tamoxifen or DCZ. Mice were given 3 doses of tamoxifen, and 5×10^5 4MOSC1 cells were implanted into the tongue. Where indicated, 0.01 mg/kg DCZ was administered daily starting one day after tumor implantation.

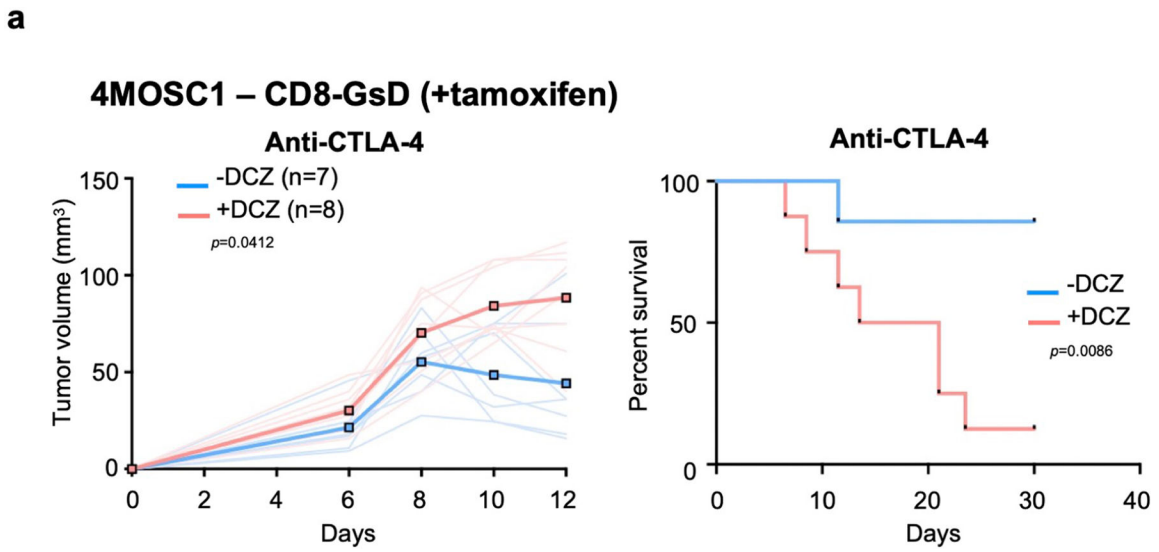

Extended Data Fig. 6 |. Anti-CTLA-4 response in CD8-GsD mice bearing 4MOSC1 tumors.
Tumor growth curve (left panel) and survival plot (right panel) of CD8-GsD mice implanted with 4MOSC1 tumors treated with anti-CTLA-4 with or without DCZ (n = 7 mice per group). Mice were given three doses of tamoxifen before orthotopic tumor implantation and

treated with checkpoint inhibitors and DCZ as previously described. Statistical significance was determined by two-way ANOVA. Statistical significance of survival data was calculated by the log-rank test.

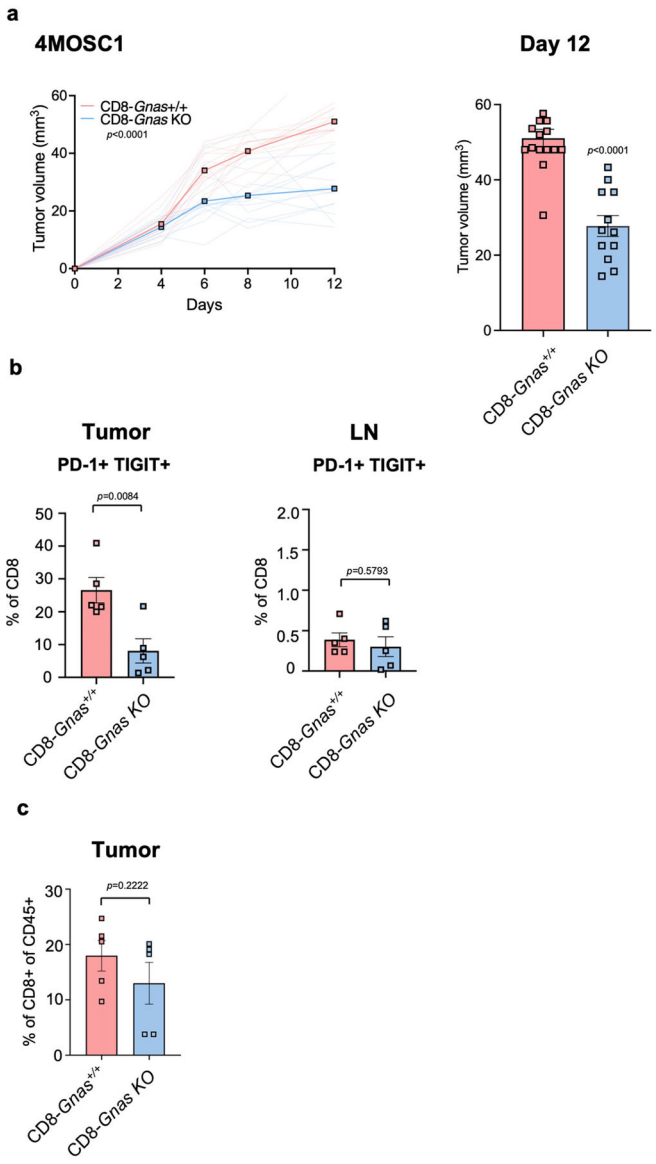

Extended Data Fig. 7 |. Effect of *Gnas* deletion CD8 T cells in mice bearing 4MOSC1 tumors. **a**, Tumor growth curve (left panel) and quantification of endpoint tumor volume (right panel) of CD8-*Gnas*+/+ (n = 14 mice) and CD8− *Gnas*−/− mice (= 12 mice) implanted with 4MOSC1 tumors. Mice were given 3 doses of tamoxifen prior to orthotopic tumor implantation. The average tumor volume and s.e.m. are shown. Statistical significance was determined by two-way ANOVA. **b**, Quantification of PD-1+TIGIT+ CD8 T cells in 4MOSC1 tumors and draining lymph nodes at endpoint. The average frequency and s.e.m. are shown (n = 5 mice per group). Statistical significance was determined by two-tailed unpaired Student's *t*-test. **c**, Frequency of CD8+ T cells in 4MOSC1 tumors in CD8-*Gnas*

KO mice versus littermate controls. The average frequency and s.e.m. are shown (n = 5 mice per group). Statistical significance was determined by two-tailed unpaired Student's *t*-test.

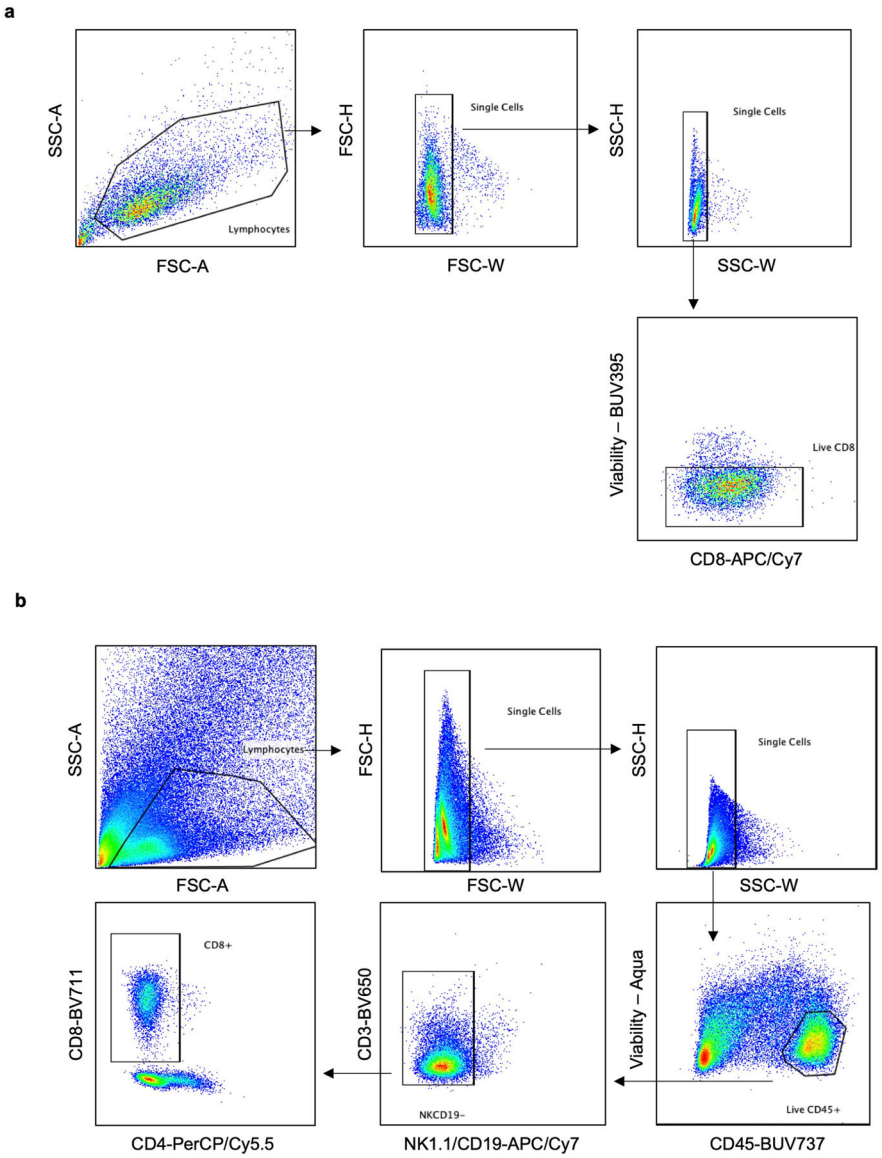

Extended Data Fig. 8 |. Gating strategy for chronic stimulation and *in vivo* experiments.
a, For chronic stimulation experiments, lymphocytes were gated from forward scatter area (FSC-A) and side scatter area (SSC-A). Single cells were distinguished from doublet cells in forward scatter height (FSC-H) and forward scatter width (FSC-W), and then side scatter height (SSC-H) and side scatter width (SSC-W). Live CD8 cells were then gated. **b**, For in vivo experiments, lymphocytes were gated from forward scatter area (FSC-A) and side scatter area (SSC-A). Single cells were distinguished from doublet cells in forward scatter height (FSC-H) and forward scatter width (FSC-W), and then side scatter height (SSC-H) and side scatter width (SSC-W). Live CD45 cells were then gated. T cells were

distinguished by NK1.1 negative, CD19 negative, and CD3 positive. CD8 T cells were then gated as CD4 negative.

Supplementary Material

Refer to Web version on PubMed Central for supplementary material.

Acknowledgements

This project was supported by grants from the National Cancer Institute (R01CA247551 and U54CA209891) and National Institute of Dental and Craniofacial Research (NIH/NIDCR, R01DE026870 and U01DE028227). V.H.W. was supported by an NRSA Training Award (NIH/NCI 1F31CA250488-01). R.S.-K. was supported by an NRSA Training Award (NIH/NIDCR F32DE029990-01). B.S.Y. was supported by the Pharmacological Sciences Training Program (5T32GM007752-40) and an NRSA Training Award (NIH/NIDCR1F31DE031961-01). J.P.M. was supported by grants from the National Cancer Institute (U24CA248457 and U24CA220341). A.T.W. was supported by grants from the National Cancer Institute (F31CA257344 and U54CA209891) and the National Library of Medicine (T15LM011271). R.B. was supported by grants from the National Institutes of Health NIDDK (R01-DK092590) and NIAMS (R01-AR-072368). We acknowledge A. Sharabi (University of California, San Diego) for gifting the MC38-OVA cell line, D. Vignali (University of Pittsburg) for gifting the *E8I*^{CreErt2} mouse model, R. Iglesias-Bartolome (National Cancer Institute) for gifting the *Gnas*-exon 1$^{fl/fl}$ and the Tet-GFP-PKI mouse models and R. Berdeaux (The University of Texas) for gifting the *ROSA26*^{LSLGsDREADD} mice. We acknowledge A. Goldrath for expertise and guidance in the study design and direction of the project.

Data availability

Gene Expression Omnibus accession numbers for the human datasets used in this study include GSE116256, GSE114727, GSE110686, GSE14018, GSE123813, GSE22898, GSE123139, GSE115978, GSE146771, GSE134520, GSE140228, GSE125449, GSE117570, GSE127465, GSE99254, GSE123813, GSE156728, GSE120575, GSE84820, GSE123235, GSE122969, GSE88987 and GSE141299. European Genome–Phenome Archive identifiers for the human datasets used in this study include EGAS00001002171, EGAS00001002486, EGAS00001002325 and EGAS00001002553. Additional information regarding these datasets can be found in Supplementary Table 1. The remaining data are available within the article and supplementary information. Source data are provided with this paper.

References

1. Okazaki T & Honjo T PD-1 and PD-1 ligands: from discovery to clinical application. Int. Immunol 19, 813–824 (2007). [PubMed: 17606980]
2. Leach DR, Krummel MF & Allison JP Enhancement of antitumor immunity by CTLA-4 blockade. Science 271, 1734–1736 (1996). [PubMed: 8596936]
3. Mellman I, Coukos G & Dranoff G Cancer immunotherapy comes of age. Nature 480, 480–489 (2011). [PubMed: 22193102]
4. Larkin J et al. Combined nivolumab and ipilimumab or monotherapy in untreated melanoma. N. Engl. J. Med 373, 23–34 (2015). [PubMed: 26027431]
5. Haslam A & Prasad V Estimation of the percentage of US patients with cancer who are eligible for and respond to checkpoint inhibitor immunotherapy drugs. JAMA Netw. Open 2, e192535 (2019). [PubMed: 31050774]
6. Hauser AS, Attwood MM, Rask-Andersen M, Schioth HB & Gloriam DE Trends in GPCR drug discovery: new agents, targets and indications. Nat. Rev. Drug Discov 16, 829–842 (2017). [PubMed: 29075003]

7. O'Hayre M, Degese MS & Gutkind JS Novel insights into G protein and G protein-coupled receptor signaling in cancer. Curr. Opin. Cell Biol 27, 126–135 (2014). [PubMed: 24508914]
8. Wu V et al. Illuminating the Onco-GPCRome: novel G protein-coupled receptor-driven oncocrine networks and targets for cancer immunotherapy. J. Biol. Chem 294, 11062–11086 (2019). [PubMed: 31171722]
9. Pierce KL, Premont RT & Lefkowitz RJ Seven-transmembrane receptors. Nat. Rev. Mol. Cell Biol 3, 639–650 (2002). [PubMed: 12209124]
10. Tokunaga R et al. CXCL9, CXCL10, CXCL11/CXCR3 axis for immune activation—a target for novel cancer therapy. Cancer Treat. Rev 63, 40–47 (2018). [PubMed: 29207310]
11. Ayers M et al. IFN-γ-related mRNA profile predicts clinical response to PD-1 blockade. J. Clin. Invest 127, 2930–2940 (2017). [PubMed: 28650338]
12. Yao C et al. Prostaglandin E_2–EP_4 signaling promotes immune inflammation through T_H1 cell differentiation and T_H17 cell expansion. Nat. Med 15, 633–640 (2009). [PubMed: 19465928]
13. Vigano S et al. Targeting adenosine in cancer immunotherapy to enhance T-cell function. Front. Immunol 10, 925 (2019). [PubMed: 31244820]
14. Valero C et al. Response rates to anti-PD-1 immunotherapy in microsatellite-stable solid tumors with 10 or more mutations per megabase. JAMA Oncol 7, 739–743 (2021). [PubMed: 33599686]
15. Andreatta M et al. Interpretation of T cell states from single-cell transcriptomics data using reference atlases. Nat. Commun 12, 2965 (2021). [PubMed: 34017005]
16. Nieto P et al. A single-cell tumor immune atlas for precision oncology. Genome Res 31, 1913–1926 (2021). [PubMed: 34548323]
17. Zheng L et al. Pan-cancer single-cell landscape of tumor-infiltrating T cells. Science 374, abe6474 (2021). [PubMed: 34914499]
18. Li H et al. Dysfunctional CD8 T cells form a proliferative, dynamically regulated compartment within human melanoma. Cell 176, 775–789 (2019). [PubMed: 30595452]
19. Zander R et al. $CD4^+$ T cell help is required for the formation of a cytolytic $CD8^+$ T cell subset that protects against chronic infection and cancer. Immunity 51, 1028–1042 (2019). [PubMed: 31810883]
20. Wherry EJ et al. Molecular signature of $CD8^+$ T cell exhaustion during chronic viral infection. Immunity 27, 670–684 (2007). [PubMed: 17950003]
21. Wherry EJ & Kurachi M Molecular and cellular insights into T cell exhaustion. Nat. Rev. Immunol 15, 486–499 (2015). [PubMed: 26205583]
22. Inoue A et al. Illuminating G-protein-coupling selectivity of GPCRs. Cell 177, 1933–1947 (2019). [PubMed: 31160049]
23. Liu C et al. Neuropilin-1 is a T cell memory checkpoint limiting long-term antitumor immunity. Nat. Immunol 21, 1010–1021 (2020). [PubMed: 32661362]
24. Andrews LP et al. A Cre-driven allele-conditioning line to interrogate CD4. Immunity 54, 2209–2217 (2021). [PubMed: 34551314]
25. Iglesias-Bartolome R et al. Inactivation of a $G\alpha_s$–PKA tumour suppressor pathway in skin stem cells initiates basal-cell carcinogenesis. Nat. Cell Biol 17, 793–803 (2015). [PubMed: 25961504]
26. Roth BL DREADDs for neuroscientists. Neuron 89, 683–694 (2016). [PubMed: 26889809]
27. Nagai Y et al. Deschloroclozapine, a potent and selective chemogenetic actuator enables rapid neuronal and behavioral modulations in mice and monkeys. Nat. Neurosci 23, 1157–1167 (2020). [PubMed: 32632286]
28. Zhang Y et al. MKP-1 is necessary for T cell activation and function. J. Biol. Chem 284, 30815–30824 (2009). [PubMed: 19748894]
29. Lang R & Raffi FAM Dual-specificity phosphatases in immunity and infection: an update. Int. J. Mol. Sci 20, 2710 (2019). [PubMed: 31159473]
30. Seo H et al. TOX and TOX2 transcription factors cooperate with NR4A transcription factors to impose CD8. Proc. Natl Acad. Sci. USA 116, 12410–12415 (2019). [PubMed: 31152140]
31. Thommen DS & Schumacher TN T cell dysfunction in cancer. Cancer Cell 33, 547–562 (2018). [PubMed: 29634943]

32. Wang Z et al. Syngeneic animal models of tobacco-associated oral cancer reveal the activity of in situ anti-CTLA-4. Nat. Commun 10, 5546 (2019). [PubMed: 31804466]
33. Sade-Feldman M et al. Defining T cell states associated with response to checkpoint immunotherapy in melanoma. Cell 175, 998–1013 (2018). [PubMed: 30388456]
34. Samstein RM et al. Tumor mutational load predicts survival after immunotherapy across multiple cancer types. Nat. Genet 51, 202–206 (2019). [PubMed: 30643254]
35. Sinha N et al. Immune Determinants of the Association between Tumor Mutational Burden and Immunotherapy Response across Cancer Types. Cancer Res 82, 2076–2083 (2022). [PubMed: 35385572]
36. Miller BC et al. Subsets of exhausted $CD8^+$ T cells differentially mediate tumor control and respond to checkpoint blockade. Nat. Immunol 20, 326–336 (2019). [PubMed: 30778252]
37. Zelenay S et al. Cyclooxygenase-dependent tumor growth through evasion of immunity. Cell 162, 1257–1270 (2015). [PubMed: 26343581]
38. Bottcher JP et al. NK cells stimulate recruitment of cDC1 into the tumor microenvironment promoting cancer immune control. Cell 172, 1022–1037 (2018). [PubMed: 29429633]
39. Pelly VS et al. Anti-inflammatory drugs remodel the tumor immune environment to enhance immune checkpoint blockade efficacy. Cancer Discov 11, 2602–2619 (2021). [PubMed: 34031121]
40. Daher C et al. Blockade of β-adrenergic receptors improves CD8+ T-cell priming and cancer vaccine efficacy. Cancer Immunol. Res 7, 1849–1863 (2019). [PubMed: 31527069]
41. Hanahan D & Weinberg RA Hallmarks of cancer: the next generation. Cell 144, 646–674 (2011). [PubMed: 21376230]
42. Saddawi-Konefka R et al. Lymphatic-preserving treatment sequencing with immune checkpoint inhibition unleashes cDC1-dependent antitumor immunity in HNSCC. Nat. Commun 13, 4298 (2022). [PubMed: 35879302]
43. Belteki G et al. Conditional and inducible transgene expression in mice through the combinatorial use of Cre-mediated recombination and tetracycline induction. Nucleic Acids Res 33, e51 (2005). [PubMed: 15784609]
44. Akhmedov D et al. G_S–DREADD knock-in mice for tissue-specific, temporal stimulation of cyclic AMP signaling. Mol. Cell. Biol 37, e00584–16 (2017). [PubMed: 28167604]
45. Stuart T et al. Comprehensive integration of single-cell data. Cell 177, 1888–1902 (2019). [PubMed: 31178118]
46. Anders S & Huber W Differential expression analysis for sequence count data. Genome Biol 11, R106 (2010). [PubMed: 20979621]
47. Love MI, Huber W & Anders S Moderated estimation of fold change and dispersion for RNA-seq data with DESeq2. Genome Biol 15, 550 (2014). [PubMed: 25516281]
48. Singh G, Inoue A, Gutkind JS, Russell RB & Raimondi F PRECOG: predicting coupling probabilities of G-protein coupled receptors. Nucleic Acids Res 47, W395–W401 (2019). [PubMed: 31143927]
49. Yu G, Wang LG, Han Y & He QY clusterProfiler: an R package for comparing biological themes among gene clusters. OMICS 16, 284–287 (2012). [PubMed: 22455463]
50. Valero C et al. Pretreatment neutrophil-to-lymphocyte ratio and mutational burden as biomarkers of tumor response to immune checkpoint inhibitors. Nat. Commun 12, 729 (2021). [PubMed: 33526794]

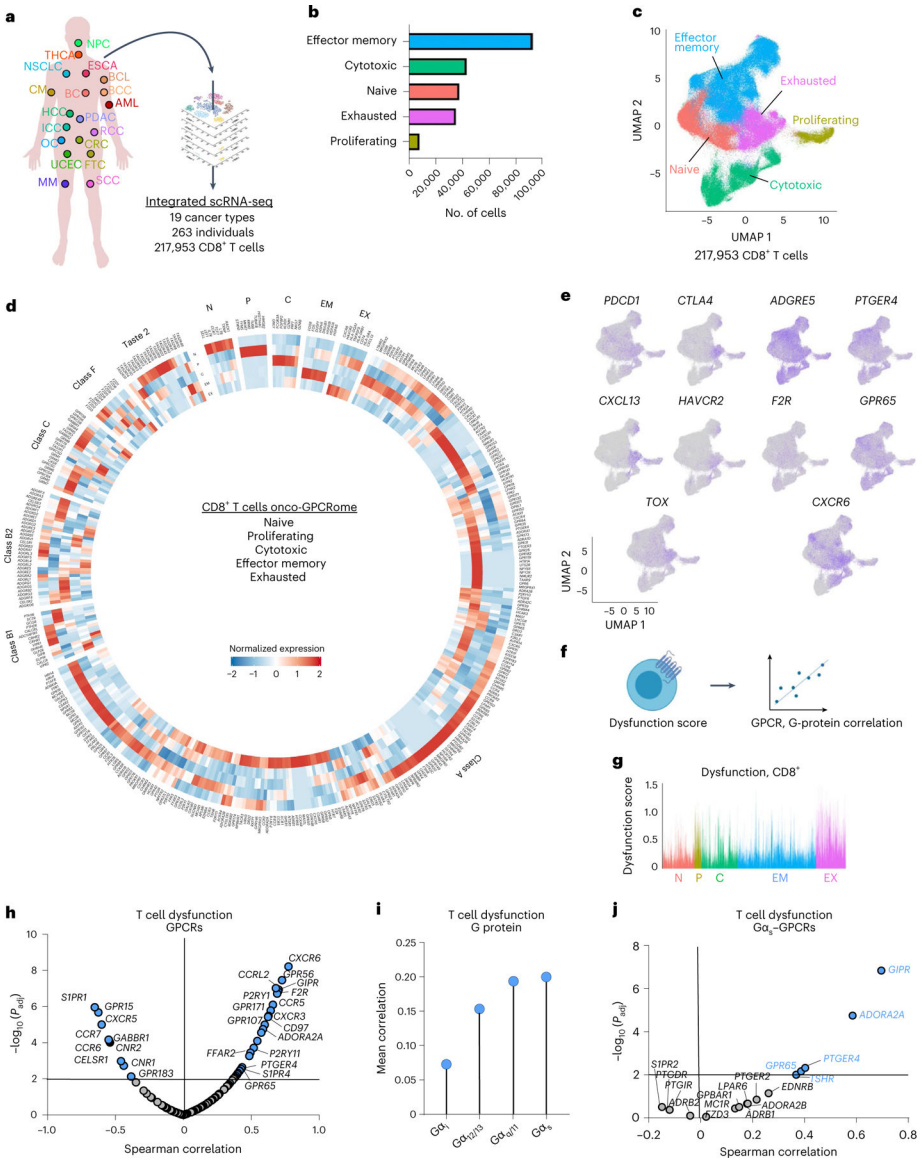

Fig. 1 |. $G\alpha_s$–GPCR correlation with T cell dysfunction and terminally exhausted T cells.

a, Schematic of integrated analysis of 19 scRNA-seq datasets (N = 263 individuals, n = 217,953 CD8$^+$ T cells). The full names of the different cancer types and their abbreviations are listed in the text and in Supplementary Table 1a. This figure was generated, in part, with BioRender.com. **b**, Integration of all CD8-expressing cells and the stratification into five different CD8$^+$ T cell subtypes (n = 217,953 CD8$^+$ T cells analyzed). **c**, Visualization of integrated CD8$^+$ T cells using dimensionality reduction. **d**, The CD8$^+$ T cell onco-GPCRome. The normalized average expression of 367 GPCR genes is shown, with blue representing lower and red representing higher expression. Genes are organized by receptor family and are aligned with annotated landmark genes from different CD8$^+$ T cell subtypes. **e**, Visualization of landmark genes for terminally exhausted CD8$^+$ T cells with the top five most highly expressed GPCRs in the terminally exhausted CD8$^+$ T cell population. **f**, Schematic explaining the correlation analysis of GPCRs and G-protein genes with the

T cell dysfunction score[18]. This figure was generated, in part, with BioRender.com. **g**, Quantification of T cell dysfunction score across all subtypes of $CD8^+$ T cells; N, naive; P, proliferating; C, cytotoxic; EM, effector memory; EX, exhausted. **h**, Spearman correlation of 119 GPCR genes with the T cell dysfunction score. Statistical *P* values were calculated and plotted from tumor-infiltrating $CD8^+$ T cells from human melanoma (GSE120575)[33]. Blue dots indicate GPCRs with Spearman correlations of $P < 0.01$, and gray dots indicate GPCRs with Spearman correlations of $P > 0.01$. A full list of *P* values and Spearman correlation values is available in Supplementary Table 1d. **i**, The mean correlation values of GPCRs were calculated based on their G-protein coupling designation from IUPHAR. These values were then ranked and plotted and included $G\alpha_i$, $G\alpha_{12/13}$, $G\alpha_{q/11}$ and $G\alpha_s$ G-protein couplings. **j**, Spearman correlation of 367 GPCR genes with the T cell dysfunction scores and the calculated statistical *P* values. $G\alpha_s$-coupled GPCRs (primary coupling as designated by IUPHAR) were plotted. Blue dots indicate GPCRs with Spearman correlations of $P < 0.01$, and gray dots indicate GPCRs with Spearman correlations of $P > 0.01$.

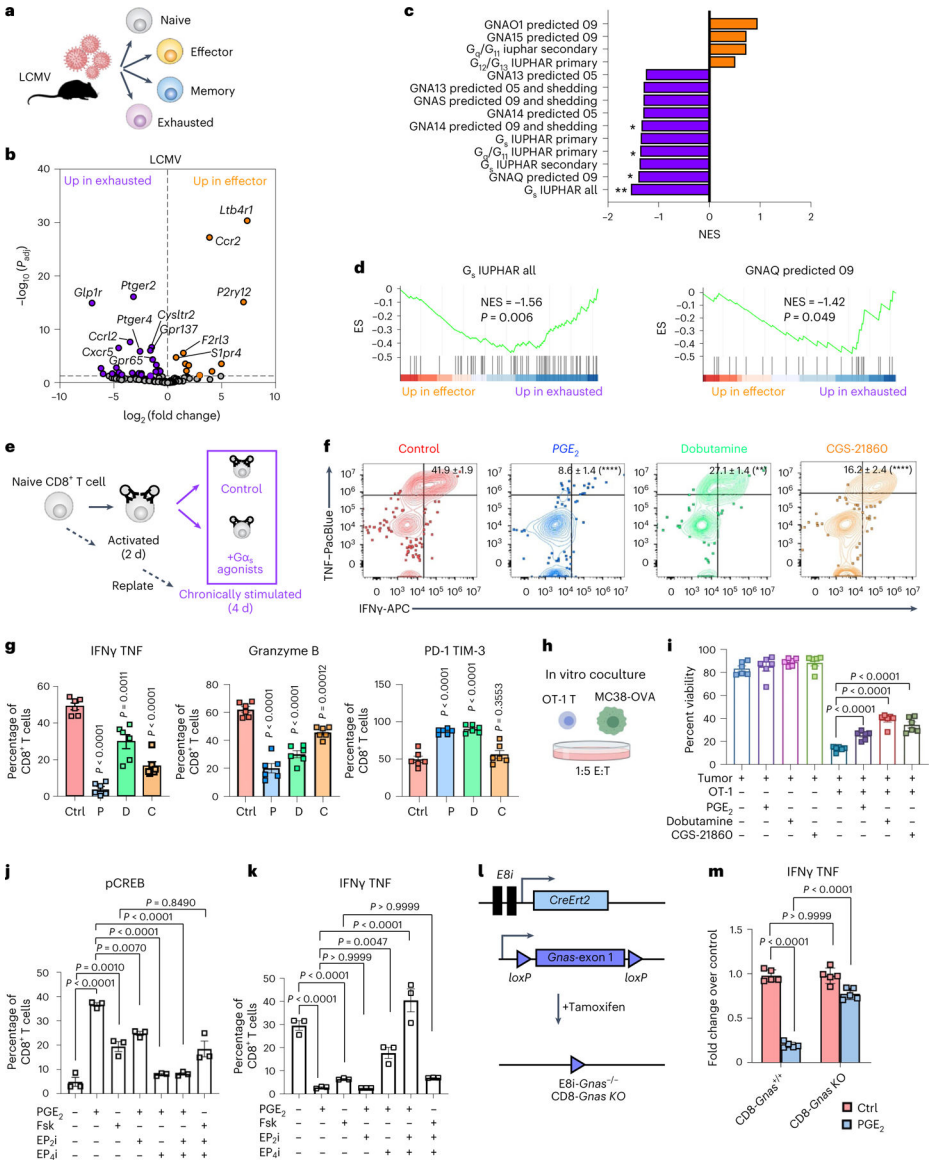

Fig. 2 |. Gα$_s$ coupling augments an exhaustion-like dysfunctional state in CD8$^+$ T cells.

a, Schematic of curated RNA-seq datasets from different subtypes of T cells sorted from the LCMV model. **b**, Differential expression analysis of GPCRs not significantly ($P >$ 0.05; gray) or significantly ($P < 0.05$) upregulated in effector (orange) versus exhausted (purple) CD8$^+$ T cells from LCMV datasets. Statistical significance was determined by the Wald test as part of the DESeq analysis package. **c**, Gene set enrichment analysis showing normalized enrichment scores (NES) of GPCRs significantly upregulated in either effector or exhausted T cells. Statistical significance was calculated as part of the gene set enrichment analysis; see Supplementary Table 3c for *P* values; *$P < 0.05$; **$P <$ 0.01. **d**, Gene set enrichment analysis mountain plots illustrating significant enrichment of gene sets from **c**; ES, enrichment score. **e**, Experimental scheme illustrating the in vitro chronic stimulation assay of CD8$^+$ T cells. **f**, Representative plots showing the expression of IFNγ and TNF in chronically stimulated CD8$^+$ T cells after treatment with Gα$_s$ agonists.

Statistical significance was determined by two-tailed unpaired Student's *t*-test comparing to control samples (see **g**); $^{**}P < 0.01$; $^{****}P < 0.0001$. **g**, Quantification of IFNγ and TNF, granzyme B, Ki-67, PD-1 and TIM-3 in $CD8^+$ T cells treated with $G\alpha_s$ agonists. The average frequency and s.e.m. are shown ($n = 6$ biologically independent samples); Ctrl, control; P, PGE_2 (1 μM); D, dobutamine (5 μM); C, CGS-21680 (5 μM). **h**, Schematic illustrating the in vitro coculture tumor killing assay. **i**, Percent killing by OT-1 T cells in the presence or absence of $G\alpha_s$ agonists. The average frequency and s.e.m. are shown ($n = 6$ biologically independent samples). **j**, Representative bar plot showing the specificity of pCREB induction (**j**) and IFNγ and TNF (**k**) inhibition by PGE_2 in the presence or absence of EP_2i or EP_4i inhibitor. The average frequency and s.e.m. are shown ($n = 3$ biologically independent samples). Statistical significance was determined by one-way analysis of variance (ANOVA). **l**, Schematic depicting the generation of *CD8-Gnas* KO mice. **m**, Quantification of IFNγ and TNF in $CD8^+$ T cells from *CD8-Gnas*$^{+/+}$ or *CD8-Gnas* KO mice. The average frequency and s.e.m. are shown ($n = 6$ biologically independent samples). Unless indicated otherwise, statistical significance was determined by two-way ANOVA. Images in **a** and **h** were generated, in part, with BioRender.com.

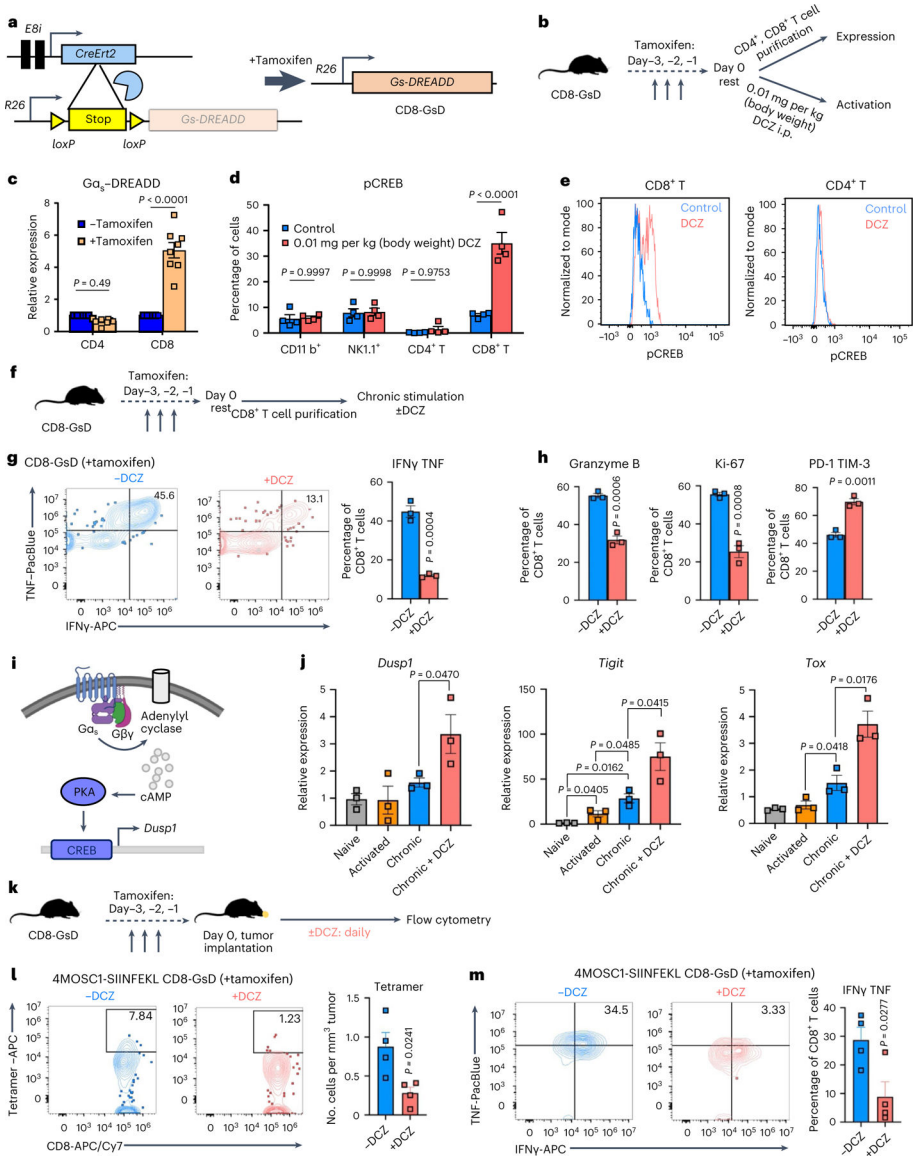

Fig. 3 |. Mechanisms of immune suppression in CD8$^+$ T cells uncovered by Gα$_s$–DREADD. **a**, Schematic illustrating the generation of CD8-GsD mice. **b**, Experimental scheme showing confirmation of expression and activation of CD8-specific Gα$_s$–DREADD by tamoxifen and DCZ, respectively. **c**, Confirmation of Gα$_s$–DREADD expression in CD4$^+$ or CD8$^+$ T cells purified from peripheral blood of CD8-GsD mice dosed with or without tamoxifen. The average relative expression and s.e.m. are shown (n = 8 mice per group). Statistical significance was determined by two-way ANOVA. **d**, Confirmation of CD8-restricted Gα$_s$–DREADD activation following tamoxifen and DCZ treatment in CD11b$^+$, NK1.1$^+$, CD4$^+$ or CD8$^+$ cells from peripheral blood. The average frequency and s.e.m. are shown (n = 4 mice per group). Statistical significance was determined by two-way ANOVA. **e**, Representative histograms showing pCREB induction from 0.002 mg ml^{-1} DCZ in vitro. **f**, Experimental scheme showing an in vitro chronic stimulation assay with CD8$^+$ T cells purified from CD8-GsD mice. **g**, Representative flow cytometry plots of IFNγ

and TNF (left) and quantification (right) in chronically stimulated $CD8^+$ T cells with or without 0.002 mg ml^{-1} DCZ. The average relative expression and s.e.m. are shown (n = 3 biologically independent samples). **h**, Quantification of granzyme B, Ki-67, PD-1 and TIM-3 in chronically stimulated $CD8^+$ T cells treated with or without 0.002 mg ml^{-1} DCZ. The average frequency and s.e.m. are shown (n = 3 mice per group). **i**, Schematic illustrating CREB activity downstream of cAMP/PKA. **j**, qPCR data showing relative expression of *Dusp1* and exhaustion-associated genes. The average frequency and s.e.m. are shown (n = 3 biologically independent samples). **k**, Experimental schematic of CD8-GsD mice implanted with 4MSOC1-SIINFEKL. **l**,**m**, Representative flow cytometry plots (left) and quantification (right) of OVA-$tetramer^+$ (**l**) or $IFN\gamma^+TNF^+$ (**m**) $CD8^+$ T cells in CD8-GsD mice implanted with 4MOSC1-OVA treated with or without 0.01 mg per kg (body weight) DCZ (n = 4 mice per group). The average frequency and s.e.m. are shown. Unless indicated otherwise, statistical significance was determined by two-tailed unpaired Student's t-test. Images in **b**,**f**,**i** and **k** were generated, in part, with BioRender.com.

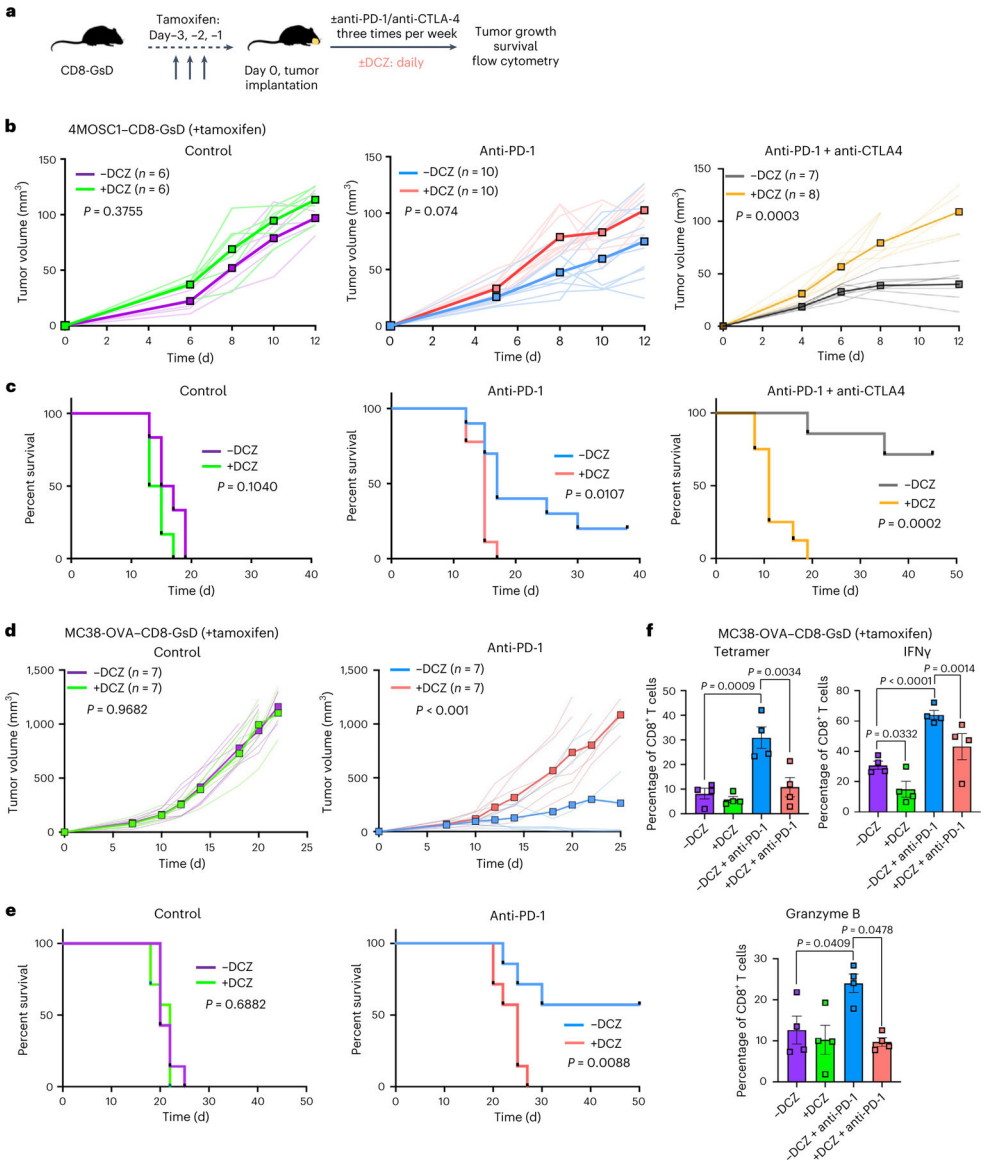

Fig. 4 |. CD8-restricted Gα$_s$ stimulation leads to immunotherapy failure.

a, Experimental scheme of CD8-GsD mice implanted with tumors and treated with DCZ, anti-PD-1 or anti-CTLA-4. This figure was generated, in part, with BioRender.com. **b**,**c**, Tumor growth curve (**b**) and survival curves (**c**) of CD8-GsD mice implanted with 4MOSC1 tumors treated with or without immunotherapy. Mice were treated with hamster IgG (left; $n = 5$ mice per group), 10 mg per kg (body weight) anti-PD-1 (middle; $n = 10$ mice per group) or both anti-PD-1 and 10 mg per kg (body weight) anti-CTLA-4 (right; $n = 7$ mice group for –DCZ and $n = 8$ mice per group for +DCZ). **d**,**e**, Tumor growth curve (**d**) and survival curves (**e**) of CD8-GsD mice implanted with MC38-OVA tumors treated with or without immunotherapy ($n = 7$ mice per group). Mice were given three doses of tamoxifen, and 1×10^5 MC38-OVA cells were implanted into the flanks of mice. Mice were treated with either hamster IgG (left) or 10 mg per kg (body weight) anti-PD-1 (middle). **f**, Mice from **d** were taken, and tumors were dissected for flow cytometric analysis. Shown is the

quantification of OVA (SIINFEKL)$^+$ (left), IFNγ^+ and granzyme B$^+$ tumor-infiltrating CD8$^+$ T cells following DCZ and/or anti-PD-1 treatment. The average frequency and s.e.m. are shown (n = 4 mice per group). Statistical significance was determined by two-way ANOVA. Statistical significance of survival data was calculated by the log-rank test.

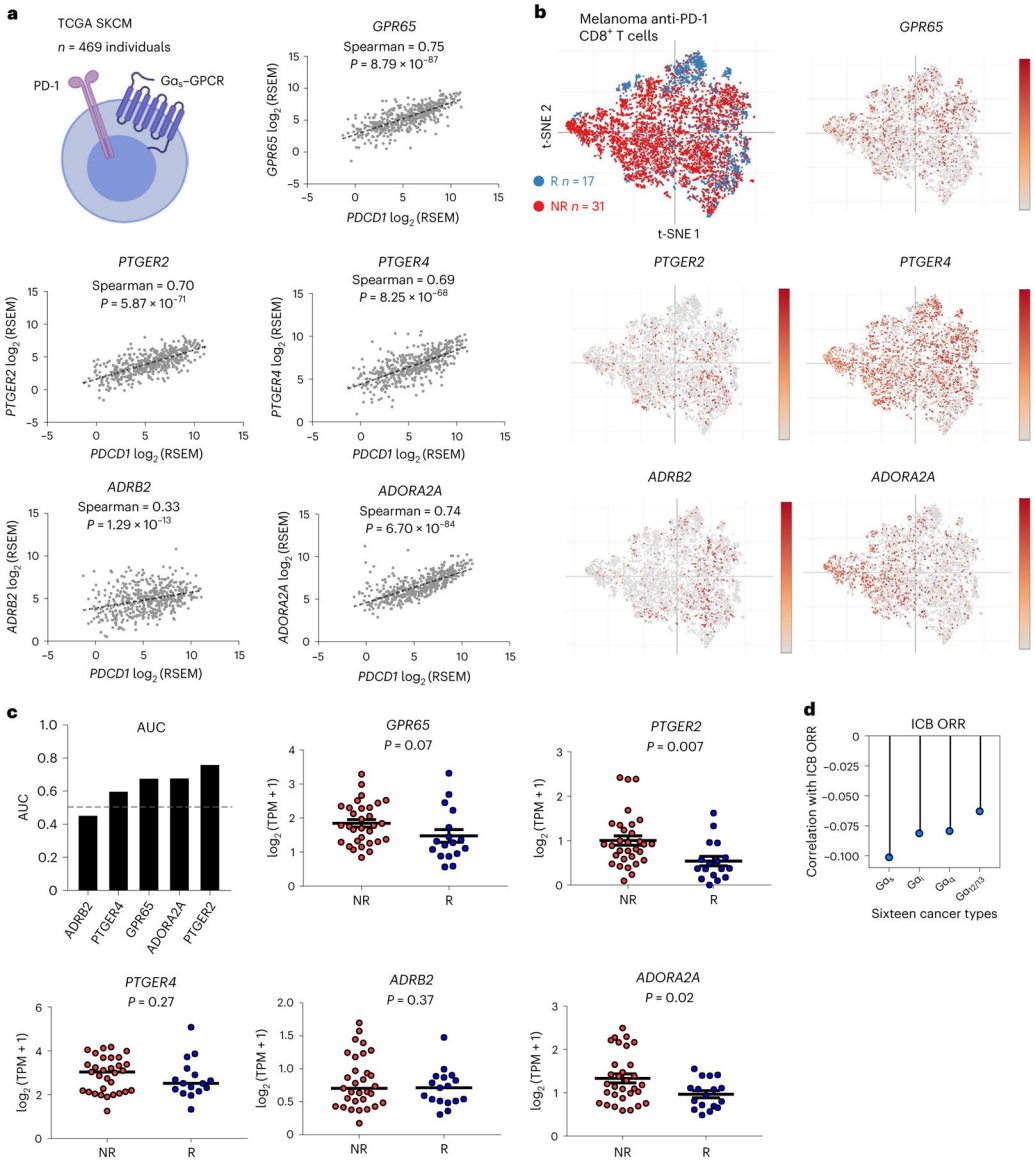

Fig. 5 |. Gα$_s$–GPCRs in individuals with cancer correlate with decreased survival and ICB response.

a, Correlation of various Gα$_s$–GPCRs to *PDCD1* in melanoma tumors from the The Cancer Genome Atlas (TCGA) skin cutaneous melanoma (SKCM) cohort (n = 469 individuals) by RNA-Seq by Expectation Maximization (RSEM) . Spearman correlations and P values are listed. This figure was generated, in part, with BioRender.com. **b**, t-Distributed stochastic neighbor embedding (t-SNE) visualization of responders (R) and non-responders (NR) to immunotherapy in individuals with melanoma from GSE120575 (top left). Expression patterns of various Gα$_s$–GPCRs are shown accordingly. **c**, AUC analysis of the ability of Gα$_s$–GPCRs to predict response to immunotherapy (top left; n = 469 individuals). GPCR expression was calculated as $\log_2$ (transcripts per million + 1), and expression levels between responders and non-responders were compared. Statistical significance was determined by two-tailed unpaired Student's t-test. The average frequency and P values are

shown. **d**, Predicted correlation of ORR to ICB for each G-protein coupling pathway across 16 cancer types.

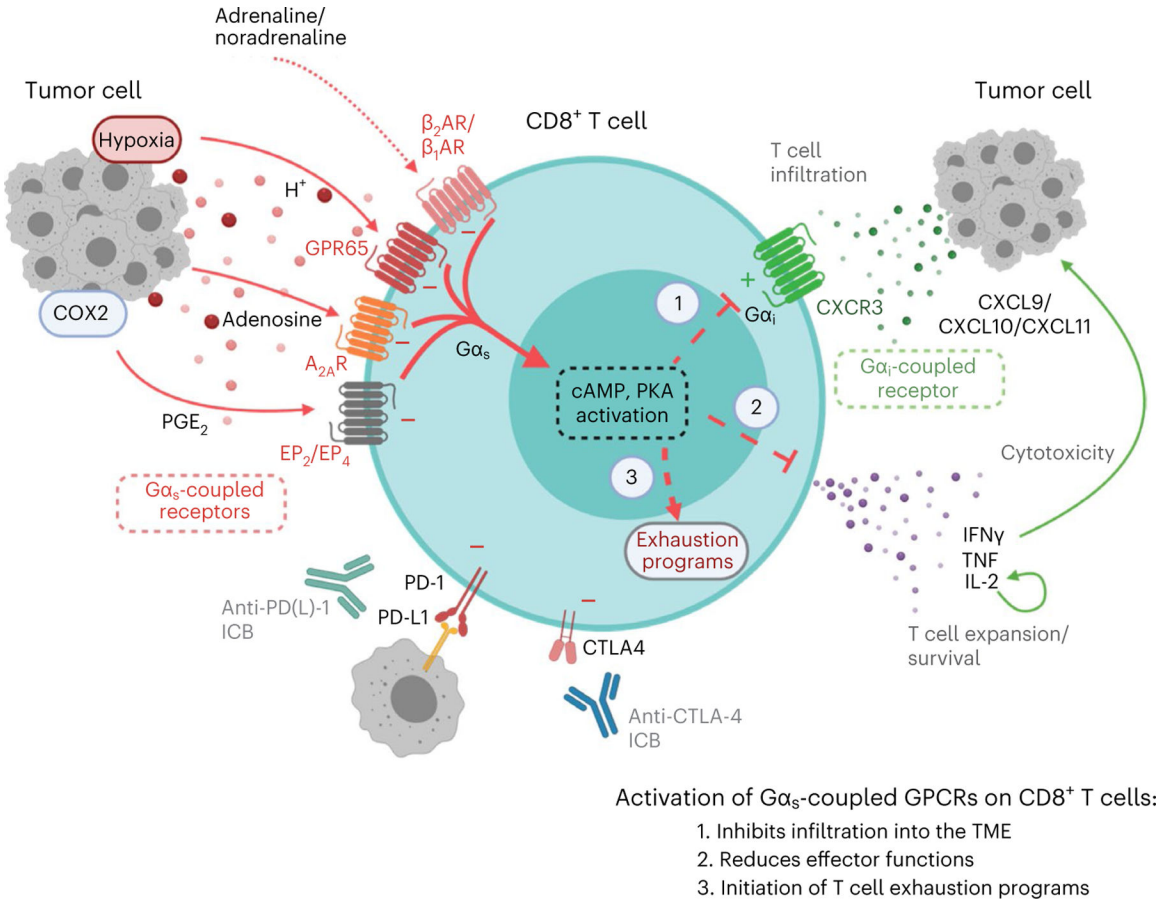

Fig. 6 |. The $G\alpha_s$ signaling axis as an immune checkpoint in cancer.

$G\alpha_s$–GPCRs, such as EP_2, EP_4, $A_{2A}R$, β_1-AR and β_2-AR, expressed on $CD8^+$ T cells have ligands in the TME which activate cAMP and PKA, augment T cell exhaustion-related programs, and diminish T cell proliferation, cytotoxicity and infiltration into the tumor. These receptors may need to be blocked in combination with PD-1 and CTLA-4 to overcome T cell dysfunction and exhaustion. This figure was generated, in part, with BioRender.com.